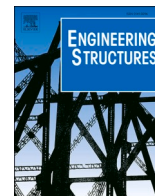# VICTORIA UNIVERSITY
MELBOURNE AUSTRALIA

Machine-learning-based predictive models for concrete-filled double skin tubular columns

This is the Published version of the following publication

Machine-learning-based predictive models for concrete-filled double skin tubular columns

Mohammadreza Zarringol [a], Vipulkumar Ishvarbhai Patel [a,*,1], Qing Quan Liang [b],
M.F. Hassanein [c], Mizan Ahmed [d]

[a] School of Engineering and Mathematical Sciences, La Trobe University, Bundoora, VIC 3086, Australia
[b] College of Engineering and Science, Victoria University, PO Box 14428, Melbourne, VIC 8001, Australia
[c] Department of Structural Engineering, Faculty of Engineering, Tanta University, Tanta, Egypt
[d] Centre for Infrastructure Monitoring and Protection, School of Civil and Mechanical Engineering, Curtin University, Kent Street, Bentley, WA 6102, Australia

ARTICLE INFO

ABSTRACT

This paper aims to develop a unique artificial neural network (ANN)-based equation as well as MATLAB- and Python-based graphical user interfaces (GUIs) using the most comprehensive and up-to-date database for predicting the behaviour of axially loaded concrete-filled double skin tubular (CFDST) short and slender columns with normal- and high-strength materials. Two machine learning (ML) methods, which are ANN and extreme gradient boosting (XGBoost), are trained and tested using 1721 sets of data, with 129 of them collected from experimental studies and 1592 generated by finite element (FE) simulations. The accuracy of the developed ML models is assessed through comparing their predictions with the experimental and FE results. To demonstrate the effect of each parameter on the predicted results, the SHapley Additive exPlanations (SHAP) method is used. The developed ML models are also used to conduct parametric studies to examine the effect of geometric and material parameters on the predicted results. The accuracy of the ML models and the proposed ANN-based equation in predicting the ultimate axial capacity of CFDST columns is compared with that of six design methods including two design code provisions and four design equations proposed by researchers. A numerical example is presented to illustrate the design procedure of the CFDST column using the proposed ANN-based equation. The results indicate that the ANN model performs better on unseen data than the XGBoost model with lower root mean square error for the test set. The results also show that the ML models and the proposed ANN-based equation are superior to the other design models in prediction accuracy.

1. Introduction

A concrete-filled double skin tubular (CFDST) column is constructed with concrete sandwiched between two metal tubes (an outer tube and an inner tube). These hollow-core composite columns share the same advantages as concrete-filled steel tubular (CFST) columns, such as good ductility, energy dissipation, and high axial capacity [1,2]. In addition, due to the hollow middle section, CFDST columns are lighter and possess higher bending stiffness and fire resistance than CFST members [3–5]. The structural behaviour of CFDST columns has been experimentally and numerically investigated by researchers. Li and Cai [6] conducted experimental and numerical studies on CFDST stub columns made of high-strength outer tube and normal-strength inner tube. It was

observed that using high-strength outer tube led to an increase in strength and ductility of the specimens. It was also shown that finite element (FE) simulation could reasonably predict the behaviour of CFDST stub columns. The effect of compressive strength of concrete on the behaviour of CFDST columns was investigated by Yan et al. [7]. Test results showed that specimens filled with higher-strength concrete exhibited lower ductility but higher initial stiffness and axial strength. In addition, increasing the yield strength and thickness of the outer tube could improve the axial strength of CFDST columns. Yan and Zhao [8] tested 24 circular CFDST stub columns and developed a formula for the prediction of the axial strength of such columns. The test observations demonstrated that the confinement effect on the sandwiched concrete in circular CFDST columns with high-strength concrete and high-strength

steel was not significant. The main failure modes of the specimens were the outward local buckling of the outer tube and inward local buckling of the inner tube.

Due to the internal hollow steel tube in CFDST columns, the confinement mechanism of CFDST columns differs from that of conventional CFST columns [4]. Although three widely used design codes, AISC 360–16 [9], Eurocode 4 [10] and AS/NZS 5100.6 [11], provide design equations for CFST columns, they do not address the design of CFDST columns. Based on the superposition method and confinement coefficient, various design formulas have been proposed by researchers for the prediction of the ultimate axial capacity of CFDST columns [8,12,13]. Generally, design equations for calculating the ultimate axial capacity of CFDST columns were derived from simplified analytical models, which were then adjusted using empirical constants to match experimental data. The literature indicates varying levels of accuracy associated with these equations. However, the machine learning (ML) models can yield higher accuracy in predicting the behaviour of structural members than conventional methods. Developing ML models such as artificial neural network (ANN) and extreme gradient boosting (XGBoost) for predicting the behaviour of structural members has been considered a reliable and robust approach [14,15]. The ML-based predictive model is capable of solving problems by identifying patterns in data. The application of ML algorithms in predicting the axial capacity of CFST columns has been well-researched. Degtyarev and Thai [16] developed and trained five boosting algorithms using 3208 test data to predict the ultimate capacity of rectangular and circular CFST columns subjected to axial compression or eccentric compression. It was observed that the ML models exhibited higher accuracy in predicting the ultimate capacity of CFST columns than existing design provisions. Hou and Zhou [17] developed and trained four predictive models using 2045 test data to predict the axial compression capacity of circular CFST columns subjected to axial compression. The results of the study showed that the ML models accurately and reliably predicted the axial capacity of circular CFST columns. Zarringol et al. [18], Naser et al. [19], Zhou et al. [20] and Ren et al. [21] have also employed ML models to determine the strengths of CFST columns. On the other hand, very limited studies have been carried out on ML models for predicting the strengths of CFDST columns. Joo and Sofi [22] used a database with 233 samples to train ANNs for estimating the axial capacity of CFDST columns with different cross-sectional shapes. They reported that the proposed ANN model could accurately ascertain the axial capacity of CFDST stub columns.

In this study, two ML algorithms, XGBoost and ANN, are employed to predict the axial capacity of circular CFDST columns fabricated with carbon steel. To train and test the ML models, the experimental results of 129 circular CFDST columns subjected to axial compression and 1592 numerical simulations generated from a validated FE model are used. The hyperparameters of the algorithms are tuned to achieve the best performance. The SHAP method is also used to identify the importance of the input features, as well as to illustrate their positive or negative effects on the predicted results. A parametric study is performed to assess the capability of the ML models in capturing the effects of the geometric and material parameters on their predictions. Using the trained ML models, an ANN-based equation and MATLAB- and Python-based GUIs are developed for predicting the ultimate axial capacity of circular CFDST short and slender columns. The accuracy of two design code provisions and four design formulas for circular CFDST columns is compared with that of the developed ML models and the proposed ANN-based equation. A numerical example is provided to illustrate the calculation of the ultimate axial capacity of CFDST short and slender columns using the proposed ANN-based equation.

2. Experimental database

To predict the ultimate axial capacity of circular CFDST columns using ML algorithms, a database consisting of 129 experimental results

was compiled. Only CFDST columns made of carbon steel without any internal stiffeners were selected. In addition, the compressive strength of the core concrete was based on the cylinder tests. If a study reported the cube compressive strength, it was converted to the compressive strength of cylinder using an expression proposed by Mansur and Islam [23]. The range of geometric and material parameters covered in the test database is shown in Fig. 1. Table 1 summarises the classification of the specimens based on the section slenderness, column slenderness, and material strengths. In the figure and table, f_c' is the compressive cylinder strength of concrete, f_y is the yield strength of the steel tube, L is the length of the column, D and t are the diameter and thickness of the steel tube, and λ^* is the section slenderness coefficient calculated as follows [9]:

$$\lambda^* = \begin{cases} D_o/t_o \left(f_{yo}/E_{so} \right) & \text{for outer steel tubes} \\ D_i/t_i \left(f_{yi}/E_{si} \right) & \text{for inner steel tubes} \end{cases} \quad (1)$$

where E_s is the modulus of elasticity of the steel material and the subscripts "o" and "i" refer to the outer and inner steel tubes, respectively. As shown in Fig. 1, while the specimens had D_o/t_o ratios ranging from 24 to 100 and D_i/t_i ratios from 16 to 55, most tests were conducted on columns with D_o/t_o and D_i/t_i ratios less than 80 and 40, respectively. The section slenderness coefficient of the outer steel tube varied between 0.04 and 0.20. However, a significant number of outer steel tubes (i.e., 95% of all columns) had compact sections (i.e., $\lambda_o^* \leq 0.15$). In the database, almost all inner steel tubes had compact sections, and only one inner steel tube had a non-compact section. The compressive strength of the sandwiched concrete ranged from 14 MPa to 100 MPa, with 73% of the specimens filled with normal strength concrete. The yield strength of the steel tubes varied from 270 MPa to 770 MPa, and most of the CFDST columns were made of normal strength materials. The length-to-diameter ratio for most columns ranged from 1 to 4.

The performance of ML models is highly dependent on the quantity and quality of the training data. For instance, training a ML model with the discussed experimental data cannot lead to satisfactory predictions for CFDST columns with non-compact inner steel tube since only one specimen in the training dataset had such characteristic. Therefore, additional CFDST columns with different geometry and material properties were simulated using the FE method to fill the gaps in the experimental database.

3. FE simulation

In this study, the FE programme ABAQUS [24] was used to develop the FE model for determining the ultimate axial capacity and behaviour of axially loaded CFDST columns. The developed FE model was then employed to generate additional data for training and testing the ML models. The details of the FE model are described as follows.

3.1. Constitutive material models for concrete

Fig. 2 shows a typical stress state for circular CFDST columns under axial compression. As can be noticed, the sandwiched concrete is subjected to the lateral pressures from the outer and inner steel tubes (i.e., f_{or} and f_{ir}), where these lateral pressures provide confinement to the sandwiched concrete [25]. In the figure, $f_{c\theta}$, $f_{o\theta}$, and $f_{i\theta}$ are the circumferential stresses of the sandwiched concrete, outer and inner steel tubes, respectively. In CFDST columns, the void ratio χ, which is defined as the ratio of the outside diameter of the inner steel tube to the inside diameter of the outer steel tube, has a significant effect on the performance of the columns. Tao et al. [26] reported that for CFDST columns with a void ratio less than or equal to 0.8, the confined state of the sandwiched concrete was the same as the core concrete in CFST columns. This means that the confinement effect on the sandwiched concrete is provided only by the outer steel tube, while the inner steel tube acts as if it stands alone. This concept has been adopted by researchers [27,28] to model stress-strain σ-ε behaviour of the sandwiched concrete in CFDST
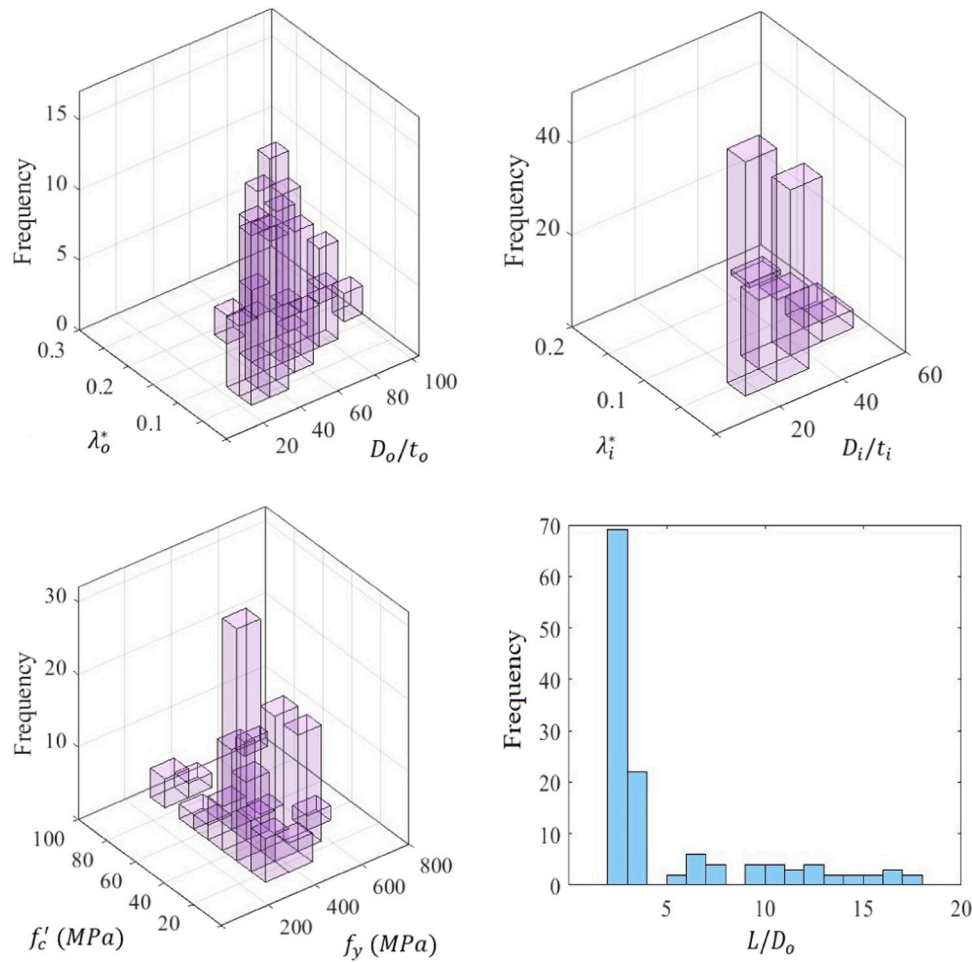
Fig. 1. Distribution of the test data.

Table 1
Classification of the specimens.

Property	Variables	Type	Ref.
Material			
	$f'_c \leq 50$ MPa	Normal strength	[71]
	$50 < f'_c \leq 100$ MPa	High-strength	[71]
	$f_y \leq 460$ MPa	Normal strength	[71]
	$460 < f_y \leq 690$ MPa	High-strength	[71]
	$f_y > 690$ MPa	Ultra-high strength	[71]
Geometry			
	$L/D_o \leq 4$	Stub columns	[72]
	$L/D_o > 4$	Slender columns	[72]
	$\lambda^* \leq 0.15$	Compact sections	[9]
	$0.15 < \lambda^* \leq 0.19$	Non-compact sections	[9]
	$\lambda^* > 0.19$	Slender sections	[9]

columns using the model proposed by Han et al. [29] for CFST columns. On the other hand, Liang [4] proposed a stress-strain model which considers the confinement effect induced by both the outer and inner steel tubes on the sandwiched concrete in a CFDST column by introducing the lateral confining pressure (f_r) taking a value between zero and 6.98 MPa. This concept has also been utilized by researchers [30, 31] for the analysis of CFDST columns. It should be mentioned that both models have been used for CFDST columns made of normal, high- and

ultrahigh- strength materials [6,7,32]. However, the Liang's model is only applicable to columns with $20 \leq D_o/t_o \leq 100$ and $15 \leq D_i/t_i \leq 55$. While the Liang's concrete model was developed using the fibre element analysis, the concrete confinement model proposed by Liang [4] can be utilized in the nonlinear finite element analysis procedures. Hassanein et al. [31] employed the concrete confinement model proposed by Liang [4] in the finite element analysis of CFDST columns.

In this study, both stress-strain models were examined and the one that provided the best fit between the simulated and experimental results was used for the FE modelling of 1592 CFDST columns. Table 2 presents the detailed expressions of the mentioned σ-ε models for circular CFDST columns, where σ and ε are the axial stress and strain of the confined concrete, respectively, $\sigma_0 = f'_c (N/mm^2)$, f'_c is the characteristic strength of the concrete, $\rho = D_o/t_o$, $\tau = D_i/t_i$, E_c is the elastic modulus of concrete, and f_{yo} and A_{so} are the yield strength and the cross-section area of the outer steel tube, respectively. The concrete damage plasticity (CDP) model available in ABAQUS was used to define the plastic mechanical properties of sandwiched concrete. The parameters that need to be defined for concrete in the CDP model are the dilation angle ψ, ratio of the second stress invariant on the tensile meridian to that on the compressive meridian K_c, flow potential eccentricity e, ratio of the compressive strength under biaxial loading to uniaxial compressive strength f_{bo}/f'_c and viscosity parameter ν. In this study, the values of ψ, K_c, e, f_{bo}/f'_c and ν were taken as $30°$, $2/3$, 0.1, 1.16 and 0.0001, respectively [6,33]. The fracture energy-based method was used to simulate the behaviour of concrete in tension. The tensile response up to 10% of f'_c was assumed to be linear [34]. Beyond that, the tensile response was modelled as follows [35]:
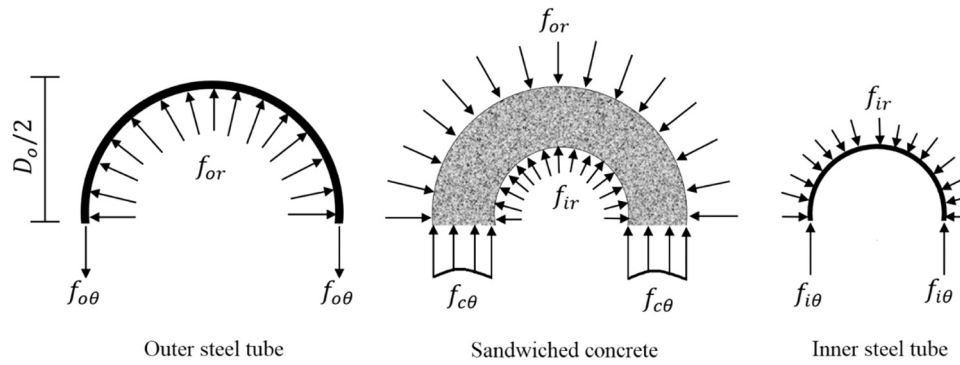
Fig. 2. Internal stresses in a CFDST column.

Table 2

Stress-strain models for confined concrete in CFDST columns with circular sections.

Equations	Ref.
$\sigma/\sigma_0 = \begin{cases} 2(\varepsilon/\varepsilon_0) - (\varepsilon/\varepsilon_0)^2 & \varepsilon/\varepsilon_0 \leq 1 \\ \dfrac{x}{\beta_0[(\varepsilon/\varepsilon_0) - 1]^2 + (\varepsilon/\varepsilon_0)} & \varepsilon/\varepsilon_0 > 1 \end{cases}$	[29]
$\beta_0 = (2.36 \times 10^{-5})^{[0.25+(\xi-0.5)^7]} f_c'^{0.5} \times 0.5 \geq 0.12$	
$\varepsilon_0 = \varepsilon_c + 800\xi^{0.2} \times 10^{-6}$	
$\xi = \dfrac{A_{so}f_{yo}}{0.25\pi f_{ck}(D_o - 2t_o)^2}$	
$\varepsilon_c = (1300 + 12.5f_c') \times 10^{-6}$	
$\sigma = \begin{cases} \dfrac{\sigma_{cc}'\lambda(\varepsilon/\varepsilon_{cc}')}{\lambda - 1 + (\varepsilon/\varepsilon_{cc}')^\lambda} & \varepsilon \leq \varepsilon_{cc}' \\ \beta_c\sigma_{cc}' + (\dfrac{\varepsilon_{cu} - \varepsilon}{\varepsilon_{cu} - \varepsilon_{cc}'})(\sigma_{cc}' - \beta_c\sigma_{cc}') & \varepsilon_{cc}' < \varepsilon \leq \varepsilon_{cu} \\ \beta_c\sigma_{cc}' & \varepsilon > \varepsilon_{cu} \end{cases}$	[4]
$\lambda = \dfrac{E_c}{E_c - (\sigma_{cc}'/\varepsilon_{cc}')}$	
$\sigma_{cc}' = \gamma_c f_c' + 4.1f_r$	
$\varepsilon_{cc}' = \varepsilon_c'(1 + 20.5\dfrac{f_r}{\gamma_c f_c'})$	
$\varepsilon_c' = \begin{cases} 0.002 & \gamma_c f_c' \leq 28MPa \\ 0.002 + \dfrac{\gamma_c f_c' - 28}{54000} & 28 < \gamma_c f_c' \leq 82MPa \\ 0.003 & \gamma_c f_c' > 82MPa \end{cases}$	
$\gamma_c = 1.85t_c^{-0.135} \quad 0.85 \leq \gamma_c \leq 1.0$	
$f_r = 8.525 - 0.166\rho - 0.00897\tau + 0.00125\rho^2 + 0.00246\rho\tau - 0.0055\tau^2 \geq 0$	
$\varepsilon_{cu} = \begin{cases} 0.03 & for \rho \leq 60 \\ 0.023 + (100 - \rho)(0.03 - 0.023)/(100 - 60) & for 60 < \rho \leq 100 \\ 0.02 & for \rho > 100 \end{cases}$	
$\beta_c = \begin{cases} 1 & \rho \leq 40 \\ k_3 & \rho > 40 \end{cases}$	
$k_3 = \begin{cases} K_3 & if K_3 \geq 0 \\ 0.0000339\rho^2 - 0.010085\rho + 1.349 & if K_3 < 0 \end{cases}$	
$K_3 = 1.73916 - 0.00862\rho - 0.04731\tau - 0.00036\rho^2 + 0.00134\rho\tau - 0.00058\tau^2$	

$$G_f = (0.0469d_{max}^2 - 0.5d_{max} + 26)(f_c'/10)^{0.7} \quad (N/m) \tag{2}$$

where G_f is the fracture energy of concrete and d_{max} is the maximum coarse aggregate size (in mm). The Poisson's ratio v_c of concrete was taken as 0.2, and the modulus of elasticity E_c of normal and high strength concrete in MPa was calculated as follows [36]:

$$E_c = \begin{cases} 5056\sqrt{f_c'} & f_c' \leq 40MPa \\ 2822\sqrt{f_c'} + 14109 & f_c' > 40MPa \end{cases} \tag{3}$$

3.2. Material model for steel

The modulus of elasticity E_s and Poisson's ratio v_s of steel were taken as 200 GPa and 0.3, respectively. An elastic-plastic model with multi-

linear hardening, as presented in Ref. [37], was utilized to define the uniaxial σ-ε behaviour of steel, with f_y ranging from 200 MP to 800 MPa. Fig. 3 shows the stages of the σ-ε model. As shown, the stress-strain relationship is linear until yielding, and then the stress remains constant between the yield strain ε_y and the strain at the beginning of strain hardening ε_p. From ε_p to the ultimate strain ε_u corresponding to the ultimate stress f_u, the stress increases in a parabola manner. In ABAQUS, the true stress-strain curve should be defined. Therefore, the engineering stress-strain curve was converted to the true stress-strain curve using the following equations [24]:

$$f_{tr} = f_{nom}(1 + \varepsilon_{nom}) \tag{4}$$

$$\varepsilon_{tr}^{pl} = \ln(1 + \varepsilon_{nom}) - f_{tr}/E_s \tag{5}$$

where f_{tr} and f_{nom} are the true and nominal steel stresses, respectively, ε_{tr}^{pl} is the true plastic strain and ε_{nom} is the nominal strain.

3.3. Element type and mesh

The sandwiched concrete was simulated using eight-node solid elements (C3D8R), and the inner and outer steel tubes were modelled using four-node shell elements with reduced integration (S4R). The selection of element type depends on the geometric complexity and behaviour of the materials being modelled. Solid elements (C3D8R) are well suited for modelling three-dimensional solid structures like concrete. They can capture complex deformations and stress distributions withing the concrete. On the other hand, shell elements (S4R) are typically used for modelling thin-walled structures like steel tubes. They are computationally efficient and can provide accurate results for modelling steel tubes. To determine an optimized mesh size, a mesh convergence study was performed. The sensitivity analysis shows that, for stub columns, the ideal mesh size is $D_o/15$ in both circumferential and longitudinal directions, while for slender columns, the ideal mesh size is $D_o/15$ and $D_o/10$ in the circumferential and longitudinal directions, respectively. Fig. 4 shows the typical FE meshes used for the analysis of the CFDST column.

3.4. Boundary conditions and loading

Rigid body constraints were utilized to tie the top and bottom surfaces to their corresponding reference points (RPs) located at lower and upper surface centres. The boundary conditions were applied to the reference points, RP1 and RP2 (see Fig. 4). At the bottom reference point (RP2), the displacement and rotation in all directions were constrained (i.e., $d_x = d_y = d_z = 0$ and $R_x = R_y = R_z = 0$). The same boundary conditions were applied to the top reference point (RP1), except that the vertical displacement (d_z) was free. The load was simulated by applying downward displacement to RP1 equivalent to 1/6th of the columns length [38].
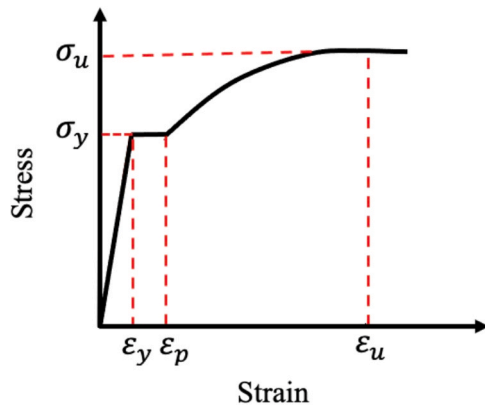

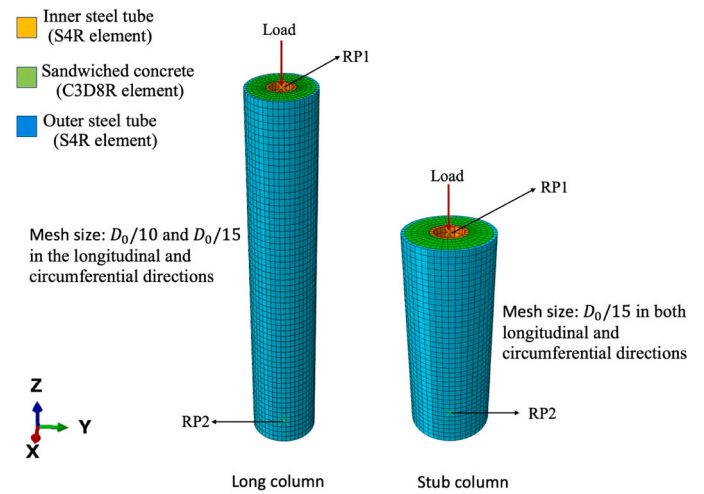**Fig. 3.** Stress-strain model of steel.

Fig. 4. Mesh of the CFDST column.

3.5. Interactions between materials and initial imperfection

The interactions between the sandwiched concrete and steel tubes were simulated using the surface-to-surface contact, where the outer and inner surfaces of the sandwiched concrete were selected as the slave surfaces, whilst the inner surface of the outer steel tube and the outer surface of the inner steel tube were set as the master surfaces [38]. The hard contact behaviour in the normal direction and the Coulomb friction model in the tangent direction with a friction coefficient of 0.6 were used in the interaction model [39]. Hard contact behaviour in the normal direction means that there is no penetration or overlap between the contacting surfaces when they come into contact. In the context of CFDST columns, this reflects the physical reality that there should be no overlapping or penetration between the concrete and steel surfaces. The Coulomb friction model is commonly used in finite element analysis to simulate the frictional interaction between materials. In the case of CFDST columns, it represents the resistance to sliding or relative motion between the concrete and steel surfaces. The initial geometric imperfection was applied to the FE model by first performing a linear eigenvalue buckling analysis of the hollow steel tubes and then using the buckling mode shape in the subsequent nonlinear analysis. The amplitudes of the imperfection was taken as $L/1000$ [33].

3.6. Verification of the FE model

In this section, the structural behaviour of the CFDST columns – specifically their ultimate axial capacities, load-deflection responses, and failure modes as predicted by the FE models – is compared with randomly selected experimental results reported by Essopjee and Dundu [40], Fan et al. [41], Yang et al. [2], Tao et al. [26], Yan et al. [7], Lu et al. [42], Li and Cai [6], Ayough et al. [43] and Zhao et al. [44]. The selected specimens covered a wide range of geometric and material properties, including the void ratios between 0.34 and 0.70, L/D ratios between 3 and 10, concrete compressive strengths between 25 MPa and 97 MPa, and steel yield strengths between 275 MPa and 770 MPa. This selection allowed for qualitative verification of the FE model. Table 3 shows the geometric and material properties of the specimens, where N_{FE} is the predicted ultimate axial capacity from the FE models and the superscripts represent the methods used to model σ-ε behaviour of the sandwiched concrete.

The results obtained from the FE models and the tests are given in Table 3. As shown, the mean values (μs) of N_{Exp}/N_{FE}^{Han} and N_{Exp}/N_{FE}^{Liang} ratios are 1.12 and 1.03, respectively, with the corresponding coefficient of variations (CoVs) of 0.09 and 0.05. It can be seen that the FE model developed based on Liang's σ-ε model [4] exhibits higher degree of

Table 3

Geometric and material properties of tested CFDST columns.

ID	$D_o \times t_o$	$D_i \times t_i$	χ	f_{yo}	f_{yi}	f'_c	N_{Exp}/N_{FE}^{Liang}	N_{Exp}/N_{FE}^{Han}	Ref.
S152.4-1.5	152.4×3	76×2	0.52	549.0	324.0	24.7	1.01	1.01	[40]
S165.1-1.5	165.1×3	76×2	0.48	516.0	324.0	24.7	1.03	1.03	
CC4 240-120	240×4	120×4	0.52	280.0	280.0	29.0	1.05	1.20	[41]
CC4 240-80	240×4	80×4	0.34	280.0	280.0	29.0	1.02	1.31	
C203-4-76	203×4	76×4	0.39	711.2	450.0	97.1	1.14	1.27	[2]
C300-6-203B	300×6	203×4	0.70	770.5	711.2	97.1	1.05	1.06	
cc5a	114×3	58×3	0.54	294.5	374.5	39.84	1.06	1.20	[26]
cc6a	240×3	114×3	0.49	275.9	294.5	39.84	0.95	1.10	
cc7a	300×3	165×3	0.56	275.9	320.5	39.84	1.04	1.09	
C4-83-0.46-3.7-2	165.2×3.69	76.4×2.80	0.48	357.7	385.6	90.7	0.93	0.99	[7]
C9-83-0.46-6.0-2	165×6.01	75.9×2.78	0.50	428.6	385.6	90.7	1.03	1.08	
C2-C4-SCC1-Ref	219.1×5.0	101.6×3.2	0.49	426	426	46.6	1.06	1.12	[42]
C2-1	356×5.50	168×3.30	0.49	618	357	39	1.01	1.01	[6]
CFDST-B0-1	165×3.0	76×3.0	0.48	309.6	324.1	38.8	1.09	1.24	[43]
O2I1	114.3×4.8	48.3×2.9	0.46	416	425	63.4	1.03	1.15	[44]
3I1	114.3×3.6	48.3×2.9	0.45	453	425	63.4	0.96	1.06	
						Mean	1.03	1.12	
						CoV	0.05	0.09	

accuracy in predicting the ultimate axial capacity of CFDST columns than the one based on Han et al. σ-ε model [29]. Fig. 5 shows the effects of the material strength and void ratio on the FE analysis results. Regarding the material strength, the FE model developed based on Liang's σ-ε model yields satisfactory results for the specimens made of normal, high- and ultrahigh-strength materials with N_{Exp}/N_{FE} ratios close to unity. In addition, the FE model developed based on Liang's σ-ε model accurately predicts the ultimate axial capacity of specimen with different void ratios. It can be concluded that the FE model implementing Liang's σ-ε model gives better results, which could be attributed to the fact that this model considers the confinement effect induced by the inner steel tube. Therefore, in this study, the σ-ε model proposed by Liang [4] was used to model 1592 CFDST columns.

Fig. 6 shows a comparison between the load (*N*) versus axial displacement (Δ) curves obtained from the FE analyses based on Liang's [4] and Han's [29] *σ-ε* models and those measured experimentally. The parameters of the specimens in the figure are presented in Table 3. It can be seen that, in general, both FE models perform well in predicting the initial stiffness of the specimens. However, the FE model utilizing the *σ-ε* model proposed by Liang [4] exhibits better performance in predicting the peak load of the specimens. Regarding the prediction of the descending branch of the load-deflection curve, the FE model based on the *σ-ε* model proposed by Han et al. [29] has relatively better performance. Overall, the discrepancy between the FE and experimental results could be attributed to the fact that FE model depends on material models that simplify the complex behaviour of concrete and steel under axial compression. These simplifications may not capture all the nonlinearities present in real materials, leading to discrepancies. The boundary conditions applied in the FE models might not perfectly replicate the actual conditions of the experiments. Small differences in how the columns were restrained or loaded could result in variations of behaviour. Variability in material properties, such as concrete compressive strength, steel yield strength, and other material

characteristics, could exist between specimens in experiments. FE models use average material properties that do not account for this variability. Experimental testing itself could have variability due to factors like fabrication tolerances, measurement errors, and environmental conditions which lead to the discrepancy between FE model predictions and experimental results [7,45].

Fig. 7 illustrates the failure modes of the specimens predicted by the FE model. The predicted failure modes of specimen C203–4-76 [2], with a L/D_o ratio of 2.96 and a χ ratio of 0.39, are outward and inward local buckling of the outer and inner tubes, respectively, which align with the experimental observations. Short CFDST columns have a relatively low slenderness ratio, which is the ratio of the column length (*L*) to its equivalent radius of gyration. As a result, the local buckling of the outer and inner steel tubes is the primary mode of failure. These short columns are less likely to experience overall buckling because their length is not sufficient to develop the necessary buckling mode across the entire column height. For specimen CFDST-B0 [43], with a L/D_o ratio of 6.06 and a χ ratio of 0.48, the predicted failure modes are the overall and local buckling, which are consistent with the test results. Slender CFDST columns have a higher slenderness ratio. Overall buckling becomes more critical in longer columns because they have greater opportunities to develop a significant lateral displacement model. When a slender column is made of non-compact or slender steel sections, it may experience the local and overall interaction buckling. This comparison indicates that the FE model accurately captures the failure modes of the specimens. It should be noted that the FE models developed based on the two mentioned concrete stress-strain models predict the same failure modes.

4. FE database

To improve the quantity and quality of the data used for training the machine learning algorithms, additional data was generated using the
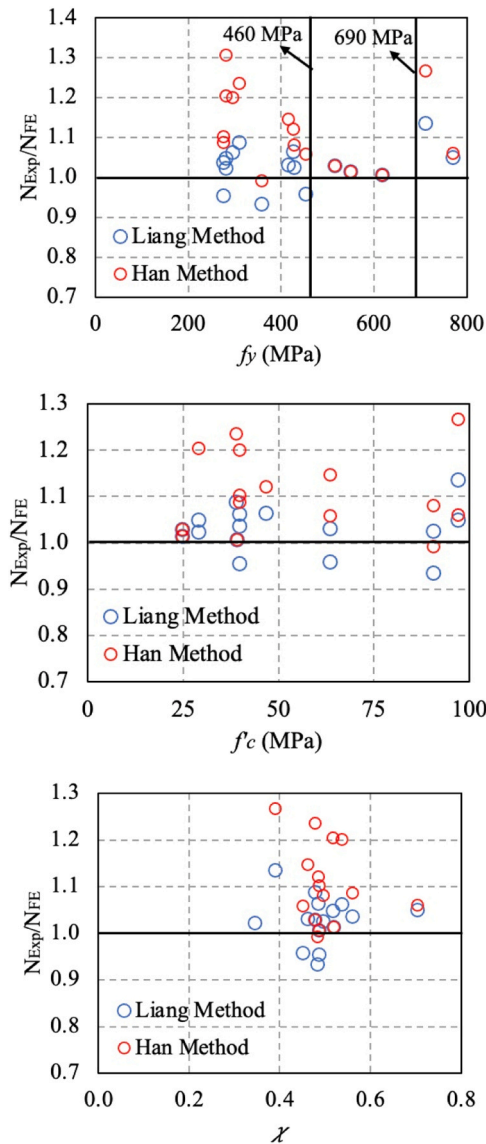
Fig. 5. Effects of the material strength and void ratio on the axial capacity.

validated FE model. A total of 1592 CFDST columns with different geometric and material properties were modelled. Fig. 8 shows the histograms of the FE database, illustrating the distribution of parameters used in the FE simulations. In the histograms, the distribution of the parameters in the experimental database is also shown for comparison purposes. It can be seen that the FE database effectively filled the gaps in the experimental dataset. The ranges of the parameters used in the FE simulations were $20 \leq D_o/t_o \leq 100$, $15 \leq D_i/t_i \leq 55$, $200 \leq f_y \leq 800$ MPa, $14 \leq f'_c \leq 100$ MPa and $1 \leq L/D_o \leq 18$. The mentioned ranges were selected based on the range of the parameters in the experimental database and the constitutive model of materials explained in the FE modelling.

5. XGBoost machine learning model

Machine learning algorithms have been successfully used to predict the capacities of the structural members. The literature suggests that XGBoost and ANN are powerful, robust and efficient ML algorithms which are capable of solving complex nonlinear problems. Therefore, in this study, XGBoost Python library [46] and MATLAB neural network toolbox [47] were used to develop the ML models for predicting the ultimate axial capacity of circular CFDST short and slender columns. In

addition, the SHAP Python library was employed to interpret the XGBoost model.

5.1. General

The XGBoost algorithm is a decision tree-based ensemble ML algorithm developed by Chen and Guestrin [48], based on the gradient boosting algorithm [49]. XGBoost consists of a set of classification and regression trees known as base learners. Each successive tree is constructed based on the errors calculated from the previous trees, resulting in a linear combination of many trees, as shown in Fig. 9. Within the XGBoost technique, a gradient descent algorithm is used to minimize errors in each iteration. Although XGBoost is a powerful ensemble learning technique, it is often treated as a "black-box" method since it does not provide explanations for its predictions [50]. This issue can be overcome by implementing explainable machine learning (XML) methods such as SHapley Additive exPlanations (SHAP). The SHAP technique introduced by Lundberg and Lee [51] is an approach based on Shapley values from the game theory [52]. Using the SHAP technique makes the XGBoost algorithm to be explainable and enables to investigate the effect of input variables on the output. For more details on the XGBoost algorithm and SHAP technique, the reader is referred to References [48,51].

5.2. Proposed XGBoost model

To evaluate the performance of the algorithm, the coefficient of determination (R^2) and Root mean square error (RMSE) were used. The eight basic parameters of D_o, t_o, D_i, t_i, L, f_{yo}, f_{yi} and f'_c were taken as inputs and N_u as an output variable. Since the parameters in the database (both the inputs and output) were not in a uniform scale, they were normalised to the range [−1 1] to prevent the model from being affected by one or few features with large values. The elastic modulus of steel and concrete were not included as inputs since their effects on the result were either minimal or considered by the basic parameters [19]. The prepared database, consisting of 129 tests and 1592 FE simulations, was randomly split into 80% training and 20% test sets [53]. The performance of XGBoost algorithm relies on the initial values of hyperparameters such as the number of trees (i.e., n_estimators) and the learning rate [54]. The hyperparameter tuning can be performed by different methods such as grid search and Bayesian optimization. The grid search method has been used by other researchers with acceptable results [55,56]. Therefore, the grid search method in combination with k-fold cross-validation (CV) was used for hyperparameters tuning in the present study. In the CV method, the training set is randomly split into k folds, where k-1 folds are used for training the algorithm and the kth fold is used as the test set. This process is repeated k times such that each fold is used exactly k-1 times for training and one time for testing. The final performance of the model is considered based on the average of RMSE calculated in each CV iteration. In this study, the value of k was set to 10 [54,57].

The initial values of hyperparameters were set as follows: n_estimators ∈ {100, 500, 1000, 2000, 3000, 5000, 10000}; maximum depth ∈ {2, 3, …, 7}, learning rate ∈ {0.001, 0.005, 0.01, 0.05, 0.1, 0.5}. The results are shown in Fig. 10. It can be seen that the XGBoost model exhibits poor performance (i.e., large RMSE values) when the learning rate is set between 0.001 and 0.01 with n_estimators at 100. With increasing n_estimators from 100 to 4000, the performance of the XGBoost model significantly improves. However, increasing n_estimators beyond 4000 does not have a significant effect on the performance of the XGBoost model. On the other hand, the XGBoost model with a learning rate between 0.05 and 0.5 achieves relatively good performance (i.e., RMSE close to zero), even though the value of n_estimators is set to 100. With increasing n_estimators from 100 to 1000, the performance of the XGBoost model starts to improve notably, with slight further improvement observed from 1000 to 4000. From 4000 to 10000 there is no
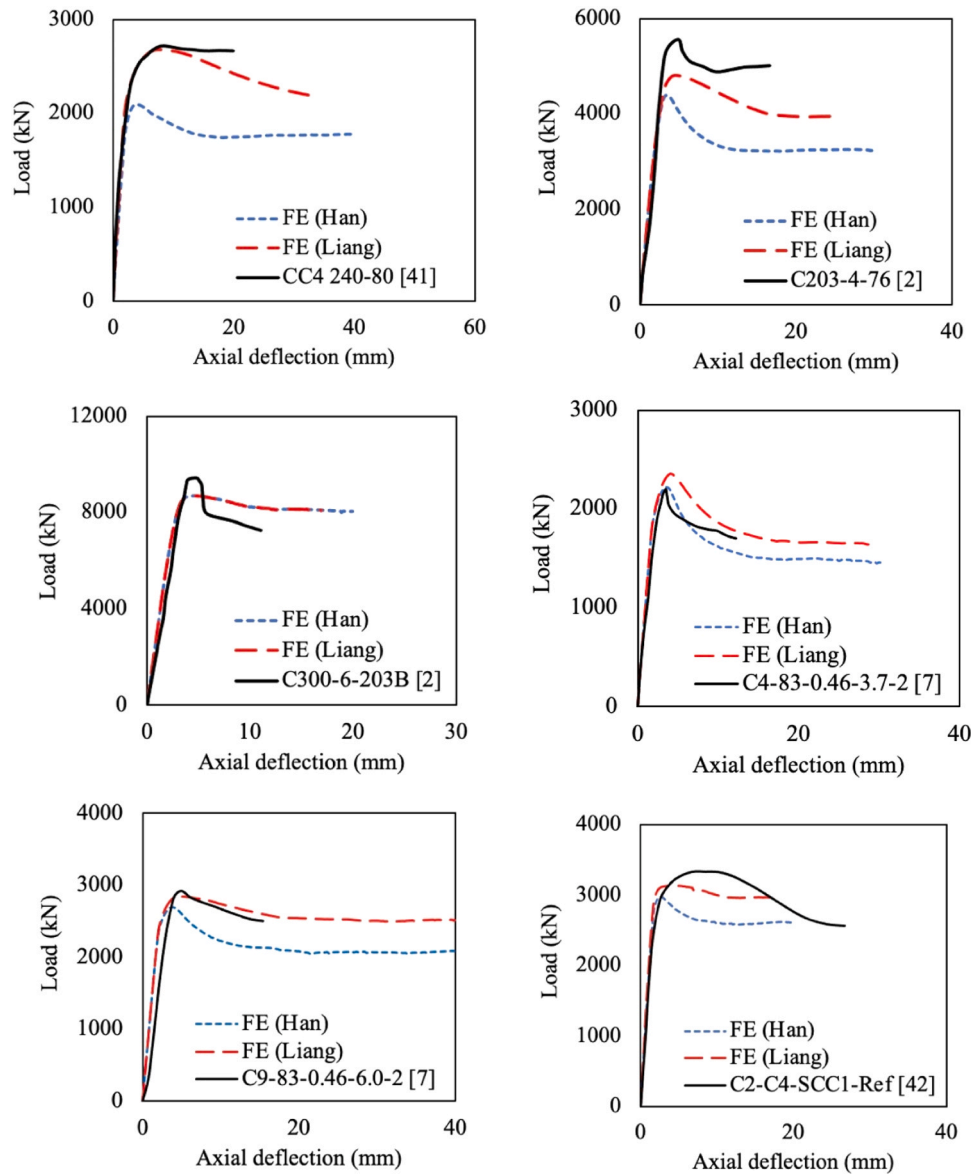
Fig. 6. Comparison between the load-deflection curves obtained from FE analyses and tests.

improvement in the performance. Another observation is that for n_estimators above 1000, increasing the learning rate from 0.05 to 0.5 has no significant effect on the performance of the XGBoost model. Regarding max_depth, it is noted that the performance of the XGBoost model is not affected by changing the max_depth from 3 to 7. Finally, the optimal values of the hyperparameters were taken as follows: n_estimators= 4000, maximum depth= 3 and learning rate= 0.05. With these settings, the 10-fold CV average RMSE for the model was 0.01542.

5.3. Performance of the XGBoost model

The performance metrics of the trained XGBoost algorithm is presented in Table 4. It can be seen that the algorithm exhibits excellent performance, with RMSE and R^2 values of 0.01086 and 0.99885, respectively. It can also be observed that the values of RMSE and R^2 for the test set are close to those for the training set, indicating that the model has acceptable performance on unseen data. Fig. 11 shows the regression plot for the training and test sets, where the identity line represents that the target and output values are identical. It can be seen that the data points are around the identity line indicating high prediction accuracy. The average ratio of $N_{Actual}/N_{u,XGBoost}$ for the FE and

experimental datasets is 1.01 and 1.00, respectively, with corresponding CoVs of 0.09 and 0.05. This suggests that the predicted values well match the actual ones. Fig. 12 shows the distribution of the percentage error (PE) for both FE and experimental databases. As shown, 78% of the predicted results corresponding to the FE database exhibit PE values less than or equal to ± 5% and only 0.3% of them have PE between ± 30% and ± 35%. These fundings indicate that the XGBoost model can predict the ultimate axial capacity of CFDST columns with a high degree of accuracy. Regarding the predicted results of the experimental database, 73% of them have PE less than or equal to ± 5% and 0.8% of the results have PE between ± 20% and ± 25%.

5.4. Interpretation of the model using SHAP values

To investigate the effect of each input feature on the XGBoost algorithm, two types of global feature importance plots were considered: (i) the SHAP feature importance plot, obtained from the average of the absolute Shapley values for each independent variable in the entire dataset, and (ii) the SHAP summary plot. Fig. 13 shows the SHAP feature importance plot, where the importance of the input features on the algorithm is arranged in descending order. It appears that the diameter of
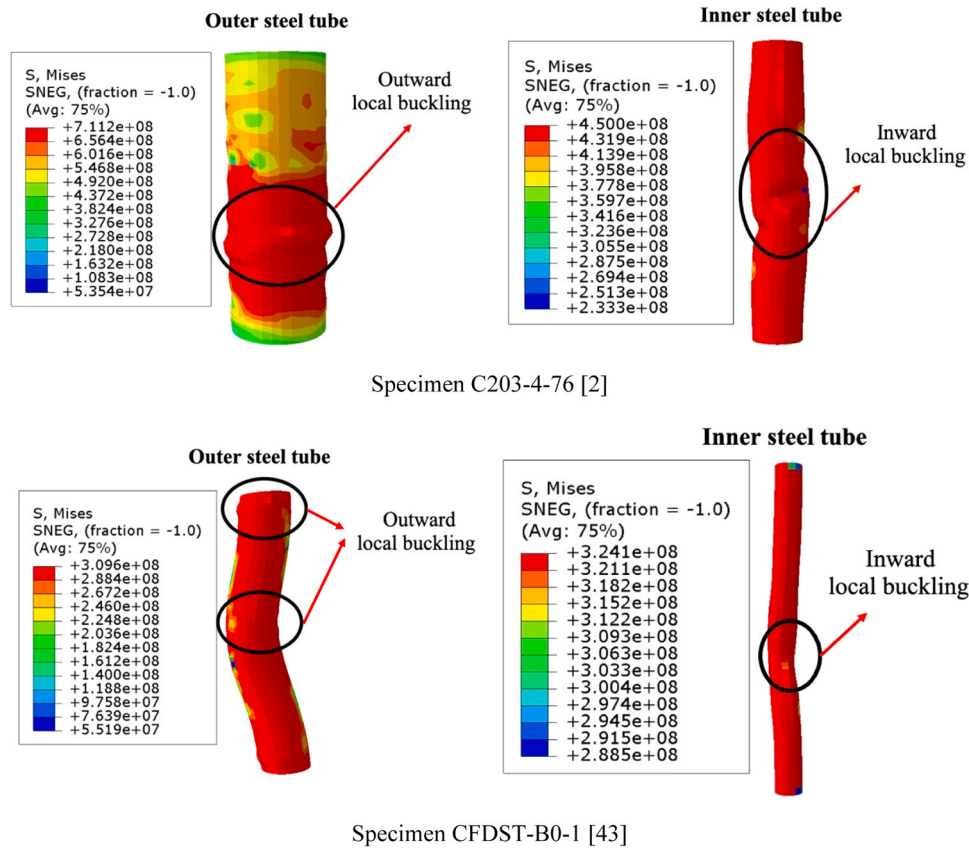
Fig. 7. Failure modes predicted by the FE simulations.

the outer steel tube has the strongest effect on the ultimate axial capacity of CFDST columns, while the effects of the other parameters on the ultimate capacity are relatively similar. To explore whether the input features had positive or negative effects on the prediction results, the SHAP summary plot was used as shown in Fig. 14. Each point on this plot is an instance of prediction, and the positive and negative SHAP values represent the positive and negative correlation between the input features and the outputs. The colour of each point also indicates the value of the input feature, ranging from low (in blue) to high (in red). Generally, it is observed that large values (i.e., red points) of all input features except D_i and L exhibit positive Shapley values, which means higher values of these parameters lead to an increase in the ultimate axial capacity of CFDST columns, while their lower values (i.e., blue points) result in a decrease in Nu. In contrast, for the diameter of the inner steel tube and the length of column, their higher values have negative Shapley values, which means that higher values of Di and L reduce the ultimate axial capacity of CFDST columns.

To investigate the effect of each input feature on the prediction for a desired specimen, the SHAP force plot has been used (i.e., local interpretation). Fig. 15 shows the force plot for the randomly selected CC4 240–120 [41], whose details are given in Table 3. Due to page limitations, only one specimen was investigated. In the figure, the base value is the average of the predictions over the training dataset, *f(x)* is the output value, the red bars represent positive SHAP values making the prediction higher and the blue bars represent negative SHAP values making the prediction lower. In addition, the length of the bar also represents the degree of importance of each input feature on the prediction. It can be observed that the diameter of the outer steel tube of the specimen has the greatest effect on pushing the prediction to a lower value than the base value, while the diameter of the inner steel tube and length of the column push the prediction towards the base value.

5.5. XGBoost-based GUI

This study developed a GUI based on the trained XGBoost model within the Python environment for the prediction of the ultimate axial capacity of CFDST short and slender columns. The GUI is presented as Supplementary Material, and its main window is shown in Fig. 16. It is important to note that this GUI can only be used for CFDST columns with geometric and material properties specified in Table 5 since the XGBoost algorithm was trained on those ranges. The user can enter numeric values for the inputs and click the "Predict" button to obtain the ultimate axial capacity. It should be mentioned that there is no need to normalise the input values, as illustrated in Fig. 16. In addition, the units of the inputs should be as follows: D_o, t_o, D_i, t_i and L in mm, and f_{yo}, f_{yi} and f'_c in MPa and the unit of the output is in kN.

6. ANN machine learning model

The architecture of an ANN model consists of a set of interconnected nodes (neurons) arranged in input, hidden and output layers. Within the artificial network, each neuron is connected to other nodes through weights. Biases are additional components of the ANN architecture, which are numeric values added to the product of inputs and weights. The computation to produce the neuron output is carried out by a linear or nonlinear function known as activation function. Three commonly used activation functions are the Logistic sigmoid (Logsig) function, hyperbolic tangent (Tansig) function and simple linear function. Fig. 17 shows a typical architecture of a single hidden layer network, where $\sum$ and $f(.)$ are the weighted sum and activation function, respectively. For more details on the ANN algorithm, the reader is referred to References [18,58–62].
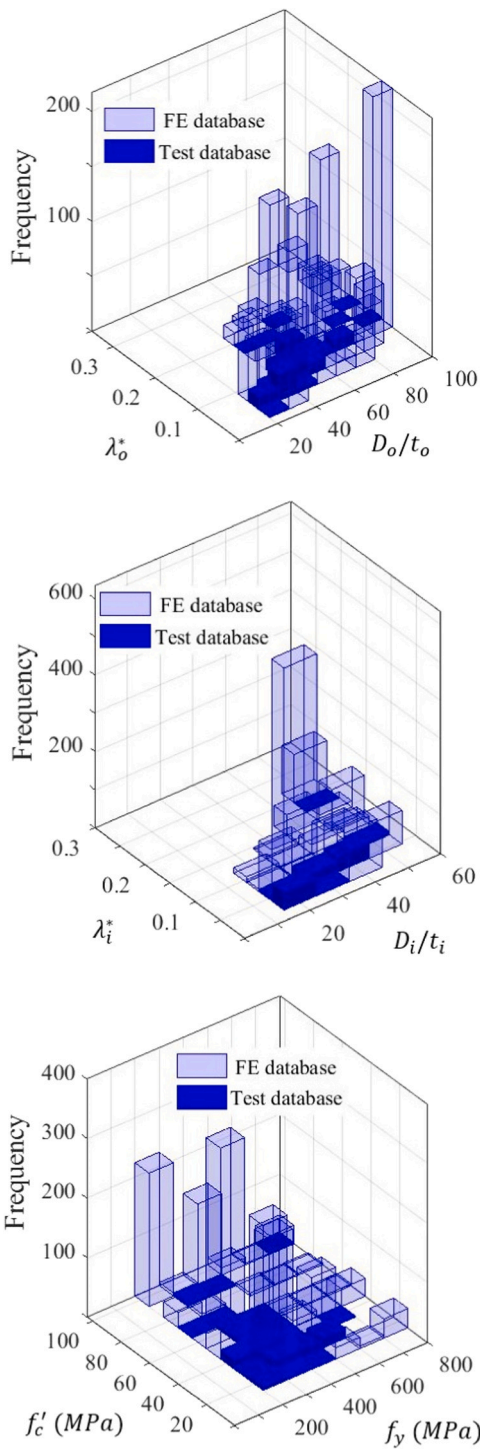
Fig. 8. Distribution of the FE data.

Fig. 9. XGBoost training process.

6.1. Proposed ANN model

The MATLAB neural network toolbox [47] was used to develop the ANN algorithm, and the performance of the algorithm was assessed using RMSE and R^2. The inputs and output of the ANN model remained the same as those in the XGBoost model described in the previous section. The input and output variables were normalised to the range $[-1$ $1]$. A feed-forward back-propagation network with the Bayesian regularization (BR) algorithm was employed as the training algorithm. The number of epochs was set to 1000 to ensure network convergence [47, 63]. The ANN model was trained a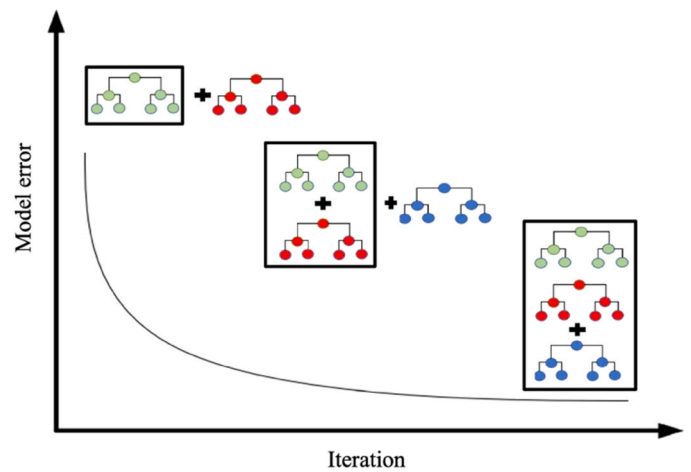nd tested using 80% and 20% of the data, respectively [47]. The Tansig and simple linear functions were used as the activation functions for the hidden and output layers. It should be noted that the superiority of the Tansig function for the hidden layer and simple linear function for the output layer compared to other functions has been stated in the literature [64,65]. To avoid complexity, one hidden layer was used to develop the neural network. To determine the number of neurons in the hidden layer, the ANN model was trained with the number of hidden layer neurons ranging from 5 to 40 in increments of 5, and the one with the lowest RMSE was selected as the best ANN model. The results are shown in shown Fig. 18. From the figure, it would appear that with 20 neurons in the hidden layer, the ANN model achieves the best performance since it has the lowest RMSE for the training and test sets. Increasing the number of hidden neurons to more than 20 leads to overfitting since RMSE of the training set decreases to a small value but RMSE of the test set increases to a large value. Therefore, the number of hidden layer neurons is chosen to be 20. Finally, to obtain an optimised trained ANN model, the developed model was run 402 times, and the model with the lowest RMSE and the highest R^2 is selected as the final model [60].

6.2. Performance of the ANN model

Fig. 19 shows the result of 402 times running of the developed ANN model. It is observed that the model at 269th iteration gives the lowest and the highest overall RMSE and R^2 values. Therefore, this model was selected as the final trained ANN model. The performance plot of the selected trained ANN model is presented in Fig. 20. The figure shows that the model successfully captures the relationship between the inputs and output with a RMSE for the training set of 0.00789 at the 363th epoch. In addition, the model does not exhibit any overfitting problem since the performance of the ANN model for the training and test sets is almost identical. The performance metrics for the ANN model are presented in Table 4. As shown, the model successfully predicts the target values (i.e., the actual values) with R^2 values of 0.99948 for the training set and 0.99904 for the test set, indicating the high accuracy of the model in predicting the ultimate axial capacity of CFDST columns. The regression plot for both training and test sets is also shown in Fig. 21. It can be observed that there is almost no deviation from the identity line, indicating high prediction accuracy and generalisation ability of the ANN model. The average ratio of $N_{Actual}/N_{u,ANN}$ for the FE and experimental datasets are 1.01 and 1.00, respectively, with corresponding CoVs of 0.14 and 0.11. The percentage error distribution of the model is given in Fig. 22. As shown, 72% of the predicted results corresponding to the FE database have PE less than or equal to $\pm 5\%$ and only 0.5% have PE between $\pm 30\%$ and $\pm 35\%$. Those percentages for the experimental data are 41% and 0.7%, respectively. A comparison between the
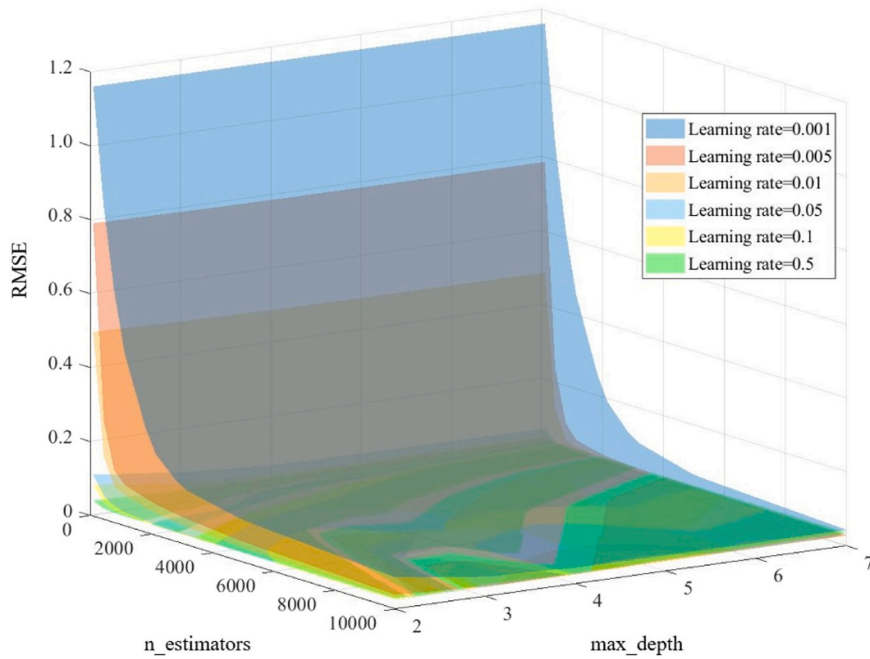
Fig. 10. Efects of n_estimators, max_depth and learning rate on the performance of the XGBooost model.

Table 4
Performance metrics for the ML models.

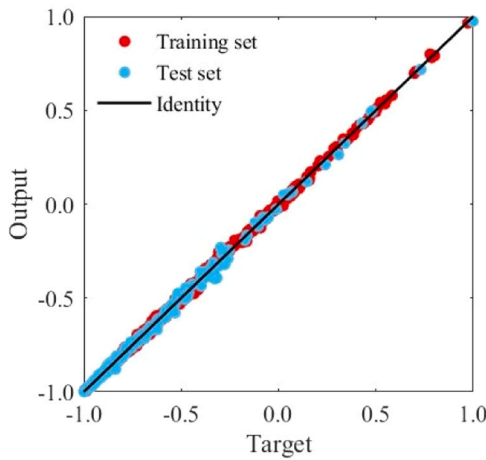| ML model	RMSE			R^2		
	Training	Test	All	Training	Test	All
XGBoost	0.00801	0.01129	0.01086	0.99940	0.99630	0.99885
ANN	0.00789	0.00948	0.00817	0.99948	0.99904	0.99938

Fig. 11. Regression plot obtained from the XGBoost model.

performance metrics of the developed ML models indicates that the ANN model has better performance in predicting the target values with a lower RMSE. The developed ANN model also shows a better prediction capability on unseen data with a lower RMSE for the test set.

6.3. ANN-based equation and GUI

Based on the trained ANN model, a GUI was developed using MATLAB for predicting the ultimate axial capacity of CFDST short and slender columns. The MATLAB-based GUI is presented as
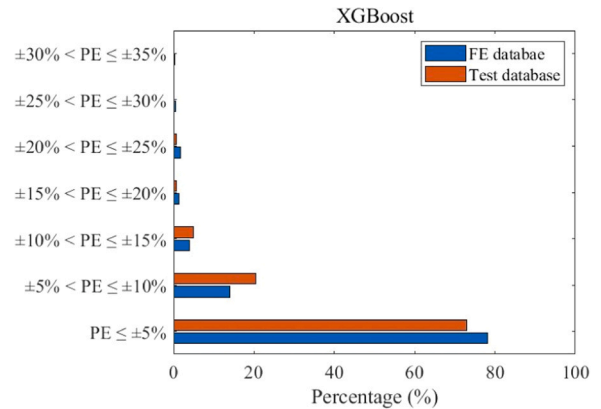

Fig. 12. Percentage error (PE) of the XGBoost model.
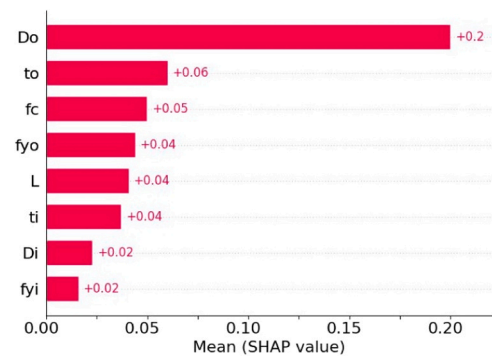

Fig. 13. SHAP feature importance plot.

Supplementary Material, and its main window is shown in Fig. 23. Similar to the Python-based GUI, it is important to note that the input values should not be normalised; they should fall within the range specified in Table 5. From the trained ANN model, a design equation was also proposed for predicting the ultimate axial capacity of CFDST
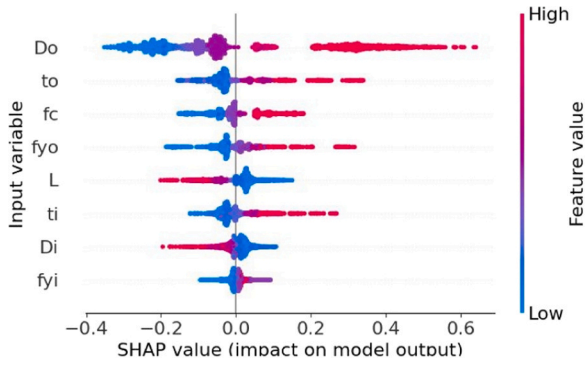
Fig. 14. SHAP summary plot.

columns, defined as follows:

$$N_u = 218774 + \sum_{j=1}^{20} \frac{Y_j}{1 + EXP(Q_j)} \tag{6}$$

$$Q_j = (a_j D_o + b_j t_o + c_j D_i + d_j t_i + e_j L + f_j f_{yo} + g_j f_{yi} + h_j f'_c + i_j) \times 10^{-7} \tag{7}$$

where j takes the values from 1 to 20 and N_u is the ultimate axial capacity in kN. The values of the constants a_j, b_j,... and i_j are given in Table 6. The obtained result from the proposed equation is the same as that of the ANN model since it is derived from the weights and biases of the trained ANN model. The units of the inputs for the GUI and deign equation should be as follows: D_o, t_o, D_i, t_i and L in mm, and f_{yo}, f_{yi} and f'_c in MPa. A numerical example based on the proposed ANN-based equation is presented in Appendix A.

7. Parametric study

A parametric study was performed to further assess the robustness of the ML models. Eight groups of circular CFDST columns were analysed using the developed ML models, and the geometric and material properties of the columns are presented in Table 7. In the parametric study, to investigate the effect of a specific parameter on the ultimate axial capacity of the columns, the value of that parameter was changed and the other ones were kept constant at their original values.

7.1. Effect of D_o/t_o ratio

To investigate the effect of the D_o/t_o ratio on the behaviour of CFDST columns, two cases were considered, one involving in which the diameter of the outer steel tubes was changed (Group 1 in Table 7), and another in which the thickness of the outer steel tubes was changed (Group 2). The results are shown in Fig. 24(a) and (b). For the case one, it can be seen that the ultimate axial capacity of CFDST columns significantly increases with increasing D_o/t_o ratio. For the case two, it can be observed that the ultimate axial capacity of CFDST columns slightly decreases with the increase in the D_o/t_o ratio. Therefore, it can be concluded that increasing the diameter of the outer steel tube is more effective in improving the ultimate axial capacity of CFDST columns

than increasing the thickness of the outer steel tube.

7.2. Effect of D_i/t_i ratio

As shown in Fig. 24(c), when the increase in the D_i/t_i ratio is due to an increase in the diameter of the inner steel tube (Group 3), the ultimate axial capacity of CFDST columns decreases. When the inner steel tube's diameter increases, it reduces the slenderness of the tube (D_i/t_i ratio increases). A larger diameter provides more resistance against buckling due to a higher moment of inertia. However, in this scenario, if the wall thickness remains the same (t_i), the tube becomes relatively less thick compared to the increased diameter. On the other hand, the decrease in the thickness of the inner steel tube (Group 4), which results in an increase in the D_i/t_i ratio, significantly decreases the ultimate axial capacity of the columns as shown in Fig. 24(d). Decreasing the thickness of the inner steel tube (t_i) results in a higher D_i/t_i ratio, which significantly increases the slenderness of the tube. A slender inner tube is less capable of resisting buckling, which is a critical mode of failure of the short columns.

7.3. Effect of f'_c

Five concrete strengths of 20, 40, 60, 80 and 100 MPa were used in the numerical analyses (see Group 5). The results are given in Fig. 24(e). In general, increasing the concrete compressive strength increases the ultimate axial capacity of the columns. An increase in concrete compressive strength (f'_c) means that the concrete is more resistant to compression forces. This enhanced material property directly contributes to the increased load-carrying capacity of the concrete.

7.4. Effect of f_y

CFDST columns in Groups 6 and 7 were analysed to investigate the effect of the yield strength of the outer and inner steel tubes on their ultimate axial capacity. Fig. 24(f) and (g) show the results. While the increase in the yield strength of the outer steel tube results in an increase in the ultimate axial capacity, the effect of the yield strength of the inner steel tube on the ultimate axial capacity is insignificant. Therefore, it can be concluded that the yield strength of the outer steel tube has a greater impact on the ultimate axial capacity of CFDST columns than the yield strength of the inner steel tube.

7.5. Effect of L/D ratio

The columns in Group 8 have L/D_o ratios ranging from 1 to 16. The results provided in Fig. 24(h) indicate that with an increase in the L/D ratio, the ultimate axial capacity of the columns decreases. The results of the parametric study indicate that the developed ML models are capable of accurately predicting the ultimate axial capacity of CFDST columns. Moreover, the predicted results for columns with different geometric and material properties align well with the findings of Liang [4,66] on the structural behaviour of CFDST columns.
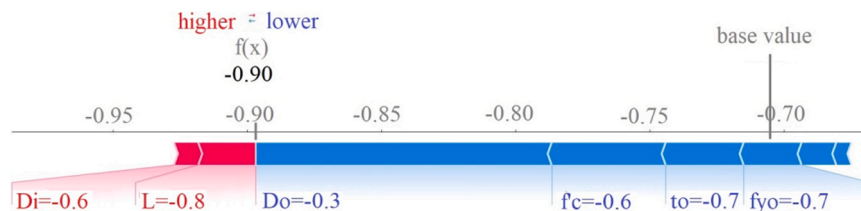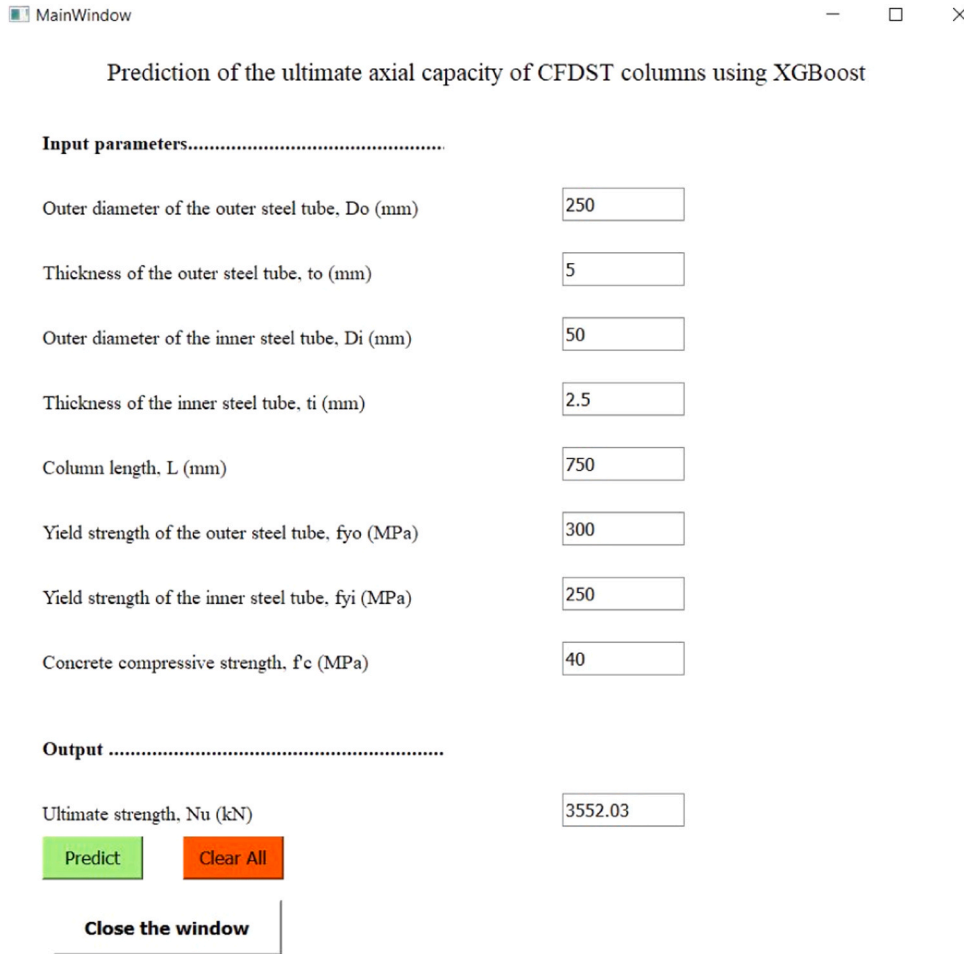

Fig. 15. Force plot.

MainWindow　　　　　　　　　　　　　　　　　　　　　　　　　　　　—　□　✕

Prediction of the ultimate axial capacity of CFDST columns using XGBoost

Input parameters...................................

Outer diameter of the outer steel tube, Do (mm)　　　　　　　| 250 |

Thickness of the outer steel tube, to (mm)　　　　　　　　　| 5 |

Outer diameter of the inner steel tube, Di (mm)　　　　　　| 50 |

Thickness of the inner steel tube, ti (mm)　　　　　　　　　| 2.5 |

Column length, L (mm)　　　　　　　　　　　　　　　　　| 750 |

Yield strength of the outer steel tube, fyo (MPa)　　　　　| 300 |

Yield strength of the inner steel tube, fyi (MPa)　　　　　| 250 |

Concrete compressive strength, f'c (MPa)　　　　　　　　| 40 |

Output ....

Ultimate strength, Nu (kN)　　　　　　　　　　　　　| 3552.03 |

[Predict]　[Clear All]

Close the window

This GUI is Developed by Mohammadreza Zarringol

School of Engineering and Mathematical Sciences, La Trobe University, Bundoora, Australia

Fig. 16. Python-based GUI.

Table 5
Values for the input parameters.

Range	D_o	D_o/t_o	D_i	D_i/t_i	χ	L/D	f_y (MPa)	f_c' (MPa)
Minimum values	100	20	15	15	0.15	1	200	14
Maximum values	500	100	440	55	0.90	18	800	100

8. Design equations for CFDST columns

Design codes such as AISC 360–16 [9] and EC4 [10] have provided design methods for CFST columns. However, they do not explicitly cover the design of CFDST columns. In this section, design equations for the calculation of the ultimate axial capacity of CFDST columns are presented based on modifications of the AISC 360–16 and EC4 equations. In addition, four different design equations for CFDST columns proposed by Hassanein and Kharoob [67], Liang [4], Yan and Zhao [8], and Uenaka et al. [12] are considered and their respective design expressions are presented in Table 8.

8.1. AISC 360-16

Considering that AISC 360–16 provides design provisions for CFST

columns, the superposition method was used to consider the contribution of the inner steel tube. This concept has been used by other researchers [2,25,68]. In addition, it was assumed that the inner steel tube does not experience local buckling before developing its full yield strength [68,69]. The modified equations are summarised in Table 8, where A_c, A_{so} and A_{si} are the cross-section areas of the sandwiched concrete, outer and inner tubes, respectively, constant K is the effective length factor, λ is the slenderness of the outer steel tube defined as the D_o/t_o ratio, λ_p and λ_r are defined as $0.15E_{so}/f_{yo}$ and $0.19E_{so}/f_{yo}$, respectively. The compact, non-compact and slender sections are respectively defined as $\lambda \geq \lambda_p$, $\lambda_p < \lambda \leq \lambda_r$ and $\lambda > \lambda_r$.

8.2. EC4

Similar to the modifications made to AISC 360–16, the superposition method was used to consider the effect of the inner steel tube on the ultimate axial capacity of CFDST columns as shown in Table 8. In the table, η_s and η_c are the coefficients to account for the confinement effect, χ is a coefficient to account for the global buckling effect and α is the imperfection factor taken as 0.21 [10].

8.3. Results and discussion

To evaluate the prediction accuracy of the six mentioned design equations, they were used to calculate the axial capacity of the CFDST
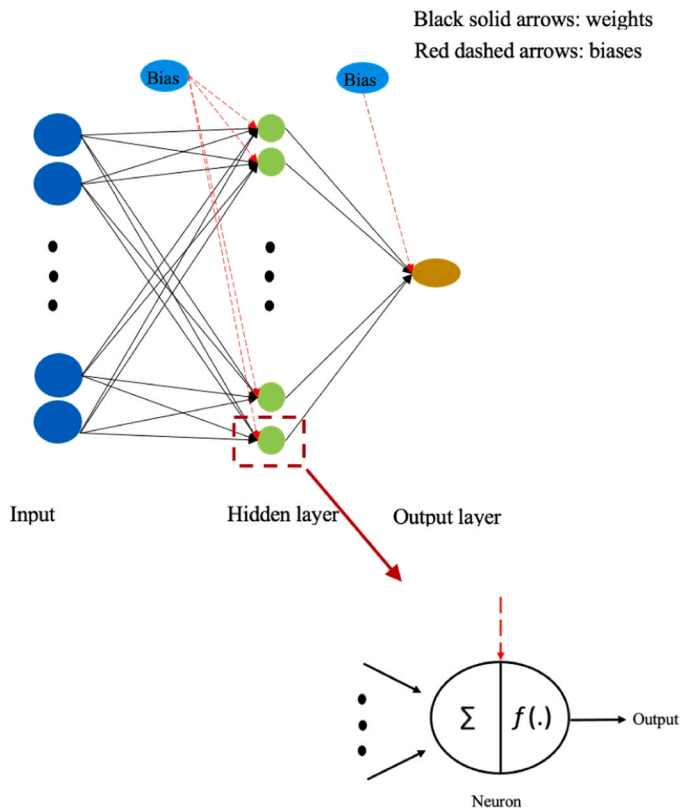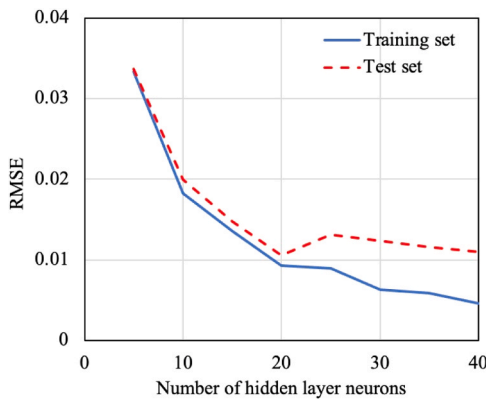
Fig. 17. A typical architecture of ANN.

Fig. 18. The optimal number neurons for the hidden layer.

Fig. 19. The results of 402 times running of the ANN model.

Fig. 20. Performance plot of the developed ANN model.
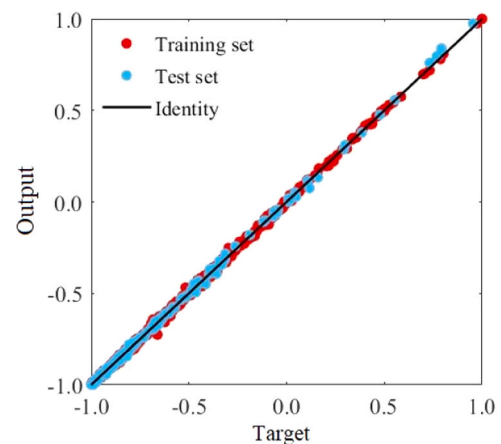
Fig. 21. Regression plot obtained from the ANN model.

columns in the database and the results were compared with the experimental and FE ones. Fig. 25 shows the comparison of the normalised ultimate axial capacity of the short and slender columns calculated using the modified code equations (i.e., Output) and the experimental and FE results (i.e., Target). In the regression plots, − 1 and + 1 refer to the minimum and maximum normalised ultimate axial capacities. From Fig. 25 it can be seen that the predictions from the modified AISC 360–16 are very conservative (i.e., most points are below the identity line) with the RMSE and R^2 values of 0.07234 and 0.95802, respectively. The average ratio of $N_{Actual}/N_{u,AISC}$ is also 1.15 with a corresponding CoV of 0.25. On the other hand, the predictions from the modified EC4 show better accuracy with the RMSE and R^2 values of 0.07108 and 0.960727, respectively and an average ratio of $N_{Actual}/N_{u,EC4}$ of 1.02 and a corresponding CoV of 0.22. However, the large CoV indicates that the predictions are widely spread from the mean. Fig. 26 shows the comparison of the normalised ultimate axial capacity of the
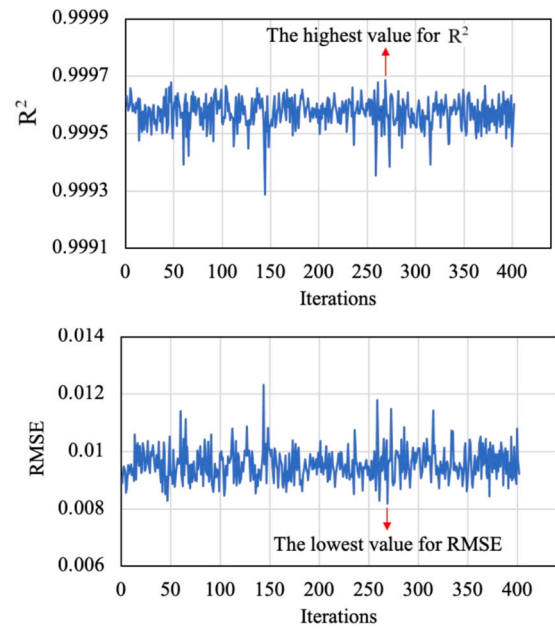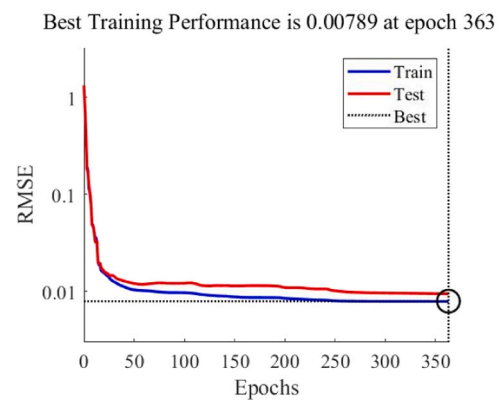
columns calculated using the equations proposed by the mentioned authors and the experimental and FE results. It should be noted that the comparison was conducted only on short columns since the equations
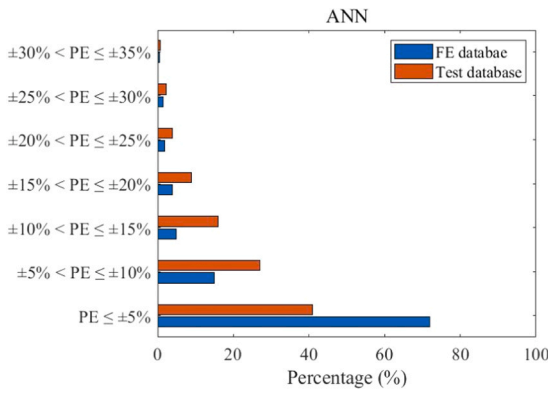
Fig. 22. Percentage error (PE) of the ANN model.

presented in the mentioned references were proposed for short columns. From Fig. 26 it can be seen that, in general, the ultimate axial capacities of the short columns predicted by the design equations are relatively in good agreement with the experimental and FE ones with the average ratio of $N_{Actual}/N_{Predicted}$ of 1.06, 1.00, 1.00 and 0.95 and corresponding CoV of 0.27, 0.19, 0.21 and 0.25 for the Hassanein and Kharoob [67], Liang [4], Yan and Zhao [8], and Uenaka et al. [12] design equations, respectively. However, the large CoV indicates that the predictions are widely spread from the mean as shown in the figure.

To facilitate a comparison between the performance of the presented predictive models, the Taylor diagram [70] was plotted as shown in Fig. 27. In the Taylor diagram, three performance metrics including standard deviation (SD), correlation coefficient (R) and RMSE are used, and the performance of each predictive model in terms of the mentioned metrics is represented by a point. In the diagram, the red curved inner lines represent RMSE, black arcs along the axes represent SD, blue radial lines represent R and the "Actual" point represents the actual observation data. From the figure, it can be seen that the performance of the ML models and the ANN-based equation is superior to that of the other
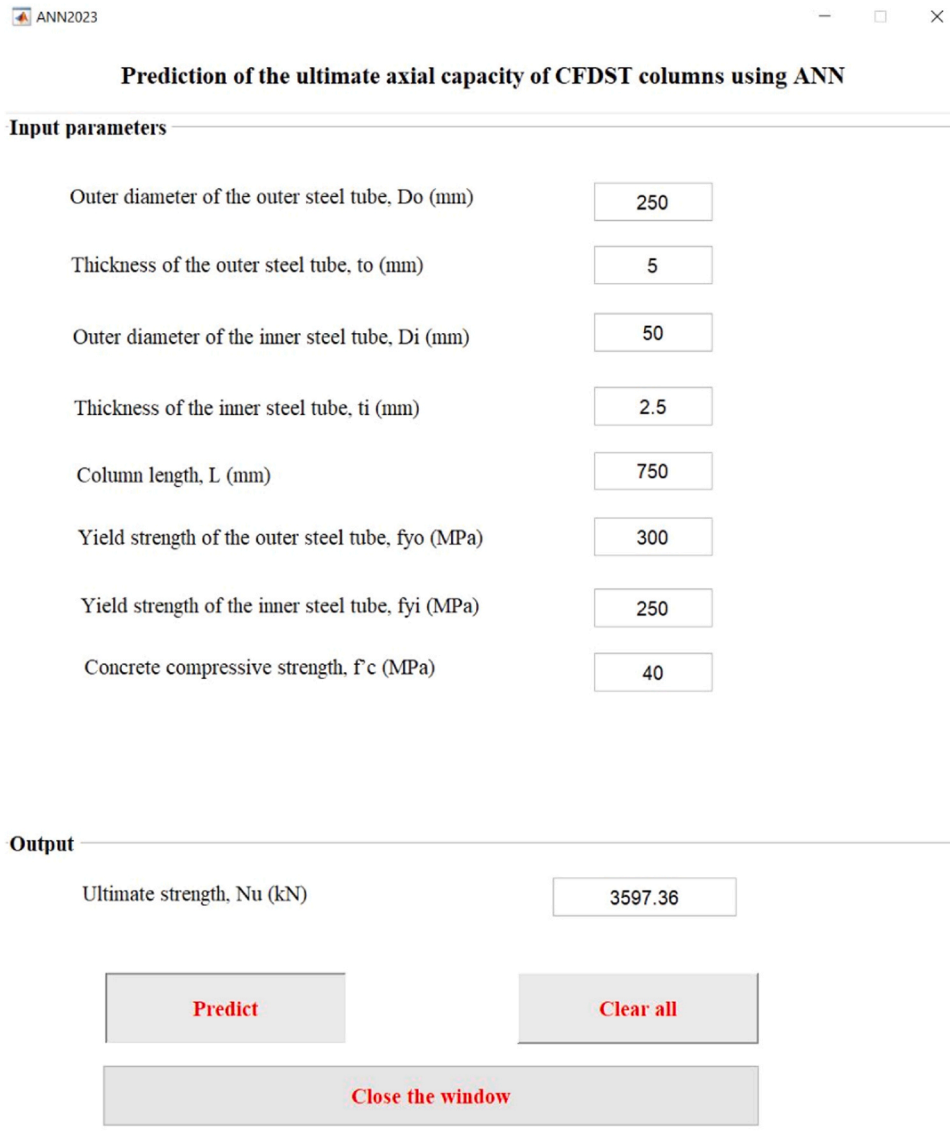
Fig. 23. MATLAB-based GUI.

Table 6
Values of the constants in the proposed equation.

j	Y_j	a_j	b_j	c_j	d_j	e_j	f_j	g_j	h_j	i_j
1	-59487	-8428	36254	-63891	147746	934	-111	-4517	52443	13947611
2	-6421	-3163	-362813	-139595	2322523	3935	-12776	1055	195190	-21594234
3	43520	-90290	-431056	32726	-590897	212	-20663	-197	-16546	70342225
4	-40751	54845	-118741	-176041	2190155	1149	5886	605	3138	-17394285
5	-121813	-43074	254052	-7765	2299537	605	-1446	-3874	7112	28568226
6	-42695	47832	-296667	-104606	-1040395	589	4937	-6905	-13226	-7880016
7	-26637	12517	-1383448	44299	-409650	2586	-11020	751	11143	-23007740
8	-27863	44269	-440401	-56866	170439	-1059	21733	19146	6773	-3121339
9	-87135	-42569	1295417	36244	-484439	-1129	-26067	876	3411	22278986
10	-30484	46724	-2139939	-43376	817662	-182	19379	3699	-20260	-21665754
11	30896	-116499	284860	89641	232961	437	-1768	980	89016	-9900236
12	-153798	55250	-223398	-27071	-427074	-1176	2807	193	24585	-29057135
13	42481	-46721	811512	34687	-495644	-1344	-39830	663	1379	31647649
14	-167592	-13797	99	-14428	14039	558	-6089	15223	1099	10662698
15	181279	18888	182704	-83539	856886	935	2444	-56	-3409	-11426681
16	-49091	-32024	-209897	114328	-659914	1940	1282	-822	-3813	4197834
17	-95953	-2128	43432	26665	455930	-174	3230	-22586	5130	-4135105
18	19781	24978	-1281684	161260	-2856354	-13	6493	-3060	9954	2814533
19	49277	62240	-855851	-25003	270801	546	-8656	-55	21688	-9666845
20	42114	-92834	149409	33394	-17275	258	356	161	58310	18028744

Table 7
Geometric and material properties of the columns used in the parametric study.

Group	ID	D_o (mm)	t_o (mm)	D_i (mm)	t_i (mm)	L (mm)	f_{yo} (MPa)	f_{yi} (MPa)	f'_c (MPa)
1	C1	250	5.00	50	2.50	750	300	250	40
	C2	275	5.00	50	2.50	750	300	250	40
	C3	300	5.00	50	2.50	750	300	250	40
	C4	325	5.00	50	2.50	750	300	250	40
	C5	350	5.00	50	2.50	750	300	250	40
2	C6	250	5.00	50	2.50	750	300	250	40
	C7	250	4.54	50	2.50	750	300	250	40
	C8	250	4.16	50	2.50	750	300	250	40
	C9	250	3.84	50	2.50	750	300	250	40
	C10	250	3.59	50	2.50	750	300	250	40
3	C11	250	5	50.0	2.50	750	300	250	40
	C12	250	5	62.5	2.50	750	300	250	40
	C13	250	5	75.0	2.50	750	300	250	40
	C14	250	5	87.5	2.50	750	300	250	40
	C15	250	5	100.0	2.50	750	300	250	40
4	C16	250	5	75	3.75	750	300	250	40
	C17	250	5	75	3.00	750	300	250	40
	C18	250	5	75	2.50	750	300	250	40
	C19	250	5	75	2.14	750	300	250	40
	C20	250	5	75	1.87	750	300	250	40
5	C21	250	5	50	2.5	750	300	250	20
	C22	250	5	50	2.5	750	300	250	40
	C23	250	5	50	2.5	750	300	250	60
	C24	250	5	50	2.5	750	300	250	80
	C25	250	5	50	2.5	750	300	250	100
6	C26	250	5	80	2.5	750	250	250	40
	C27	250	5	80	2.5	750	300	250	40
	C28	250	5	80	2.5	750	350	250	40
	C29	250	5	80	2.5	750	400	250	40
	C30	250	5	80	2.5	750	450	250	40
7	C31	250	5	100	2.5	750	300	250	40
	C32	250	5	100	2.5	750	300	300	40
	C33	250	5	100	2.5	750	300	350	40
	C34	250	5	100	2.5	750	300	400	40
	C35	250	5	100	2.5	750	300	450	40
8	C36	250	5	100	2.5	250	300	250	40
	C37	250	5	100	2.5	1000	300	250	40
	C38	250	5	100	2.5	2000	300	250	40
	C30	250	5	100	2.5	4000	300	250	40

design equations since their representative points are much closer to the "Actual" point. In addition, it can be seen that the point corresponding to the proposed ANN-based equation almost coincides with that of the ANN model indicating that the proposed equation has the same accuracy as the ANN model.

9. Conclusions

This paper has presented the XGBoost- and ANN-based machine learning models for predicting the behaviour of axially loaded CFDST short and slender columns made of normal- and high-strength materials. In total, 1721 samples (i.e., 129 tests and 1592 FE simulations) were
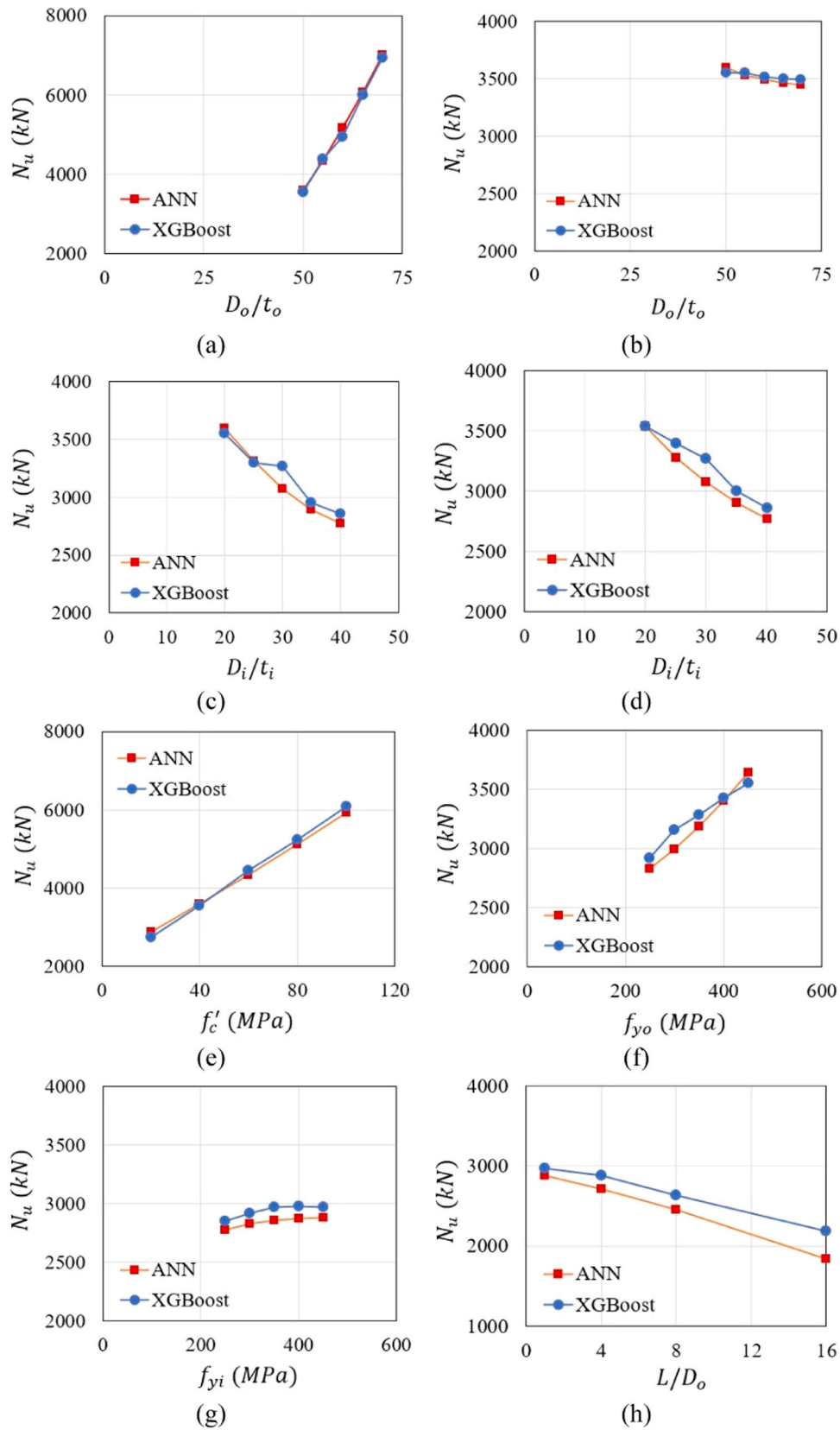
Fig. 24. Results of the parametric study.

Table 8

Design equations for CFDST columns based on AISC 360–16 and EC4.

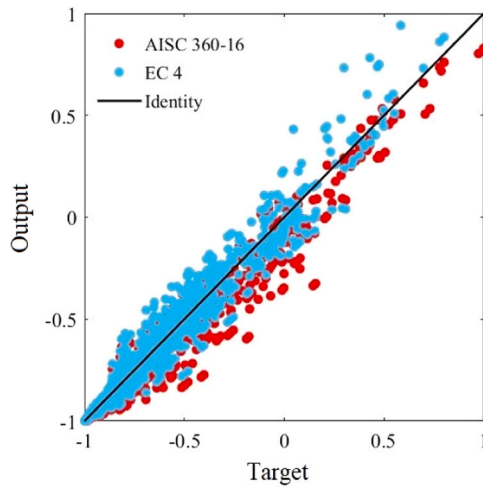| Source	Design equations
AISC 360-16[9]	$N_{u,AISC} = \begin{cases} N_n\left[0.658^{\frac{N_n}{N_{e,AISC}}}\right] & \text{for } \dfrac{N_n}{N_{e,AISC}} \leq 2.25 \\ 0.877 N_{e,AISC} & \text{for } \dfrac{N_n}{N_{e,AISC}} > 2.25 \end{cases}$
	$N_n = \begin{cases} N_p + A_{si}f_{yi} & \text{for compact sections} \\ N_p - \dfrac{N_p - N_y}{(\lambda_r - \lambda_p)^2}(\lambda - \lambda_p)^2 + A_{si}f_{yi} & \text{for noncompact sections} \\ N_s + A_{si}f_{yi} & \text{for slender sections} \end{cases}$
	$N_p = A_{so}f_{yo} + 0.95 A_c f_c'$
	$N_y = A_{so}f_{yo} + 0.7 A_c f_c'$
	$N_s = N_{cr,AISC}A_{so} + 0.7f_c'A_c$
	$N_{cr,AISC} = \dfrac{0.72 f_{yo}}{[(D_o/t_o)(f_{yo}/E_{so})]^{0.2}}$
	$N_{e,AISC} = \dfrac{\pi^2 (EI)_{eff,AISC}}{(KL)^2}$
	$(EI)_{eff,AISC} = E_{so}I_{so} + k_1 E_c I_c + E_{si}I_{si}$
	$k_1 = 0.45 + 3\left(\dfrac{A_{so}}{A_c + A_{so}}\right) \leq 0.9$
EC4[10]	$N_{u,EC4} = \begin{cases} \chi(A_{so}f_{yo} + A_c f_c' + A_{si}f_{yi}) & \text{if } \lambda_r > 0.5 \\ \chi\left[\eta_s A_{so}f_{yo} + A_c f_c'\left(1 + \eta_c\dfrac{t_o f_{yo}}{D_o f_c'}\right) + A_{si}f_{yi}\right] & \text{if } \lambda_r \leq 0.5 \end{cases}$
	$\chi = \dfrac{1}{\phi + \sqrt{\phi^2 - \lambda_r^2}} \leq 1$
	$\phi = 0.5[1 + \alpha(\lambda_r - 0.2) + \lambda_r^2]$
	$\lambda_r = \sqrt{N_{us}/N_{e,EC4}}$
	$N_{us} = A_{so}f_{yo} + 0.85 A_c f_c' + A_{si}f_{yi}$
EC4[10]	$N_{e,EC4} = \dfrac{\pi^2 (EI)_{eff,EC4}}{(KL)^2}$
	$(EI)_{eff,EC4} = E_{so}I_{so} + 0.6 E_c I_c + E_{si}I_{si}$
	$\eta_c = 4.9 - 18.5\lambda_r + 17\lambda_r^2 \geq 0 \quad \eta_s = 0.25(3 + 2\lambda_r) \leq 1$
Hassanein and Kharoob[67]	$N_{u,Hassanein} = \begin{cases} \left(1 + 0.3\dfrac{\xi}{1+\xi}\Omega\right)\left(A_{so}f_{yo} + A_c f_{cc}'\right) + A_{si}f_{yi} & \text{if } D_o/t_o \leq 150 \\ A_{so}f_{yo} + 0.85 A_c f_c' + A_{si}f_{yi} & \text{if } D_o/t_o > 150 \end{cases}$
	$\xi = \dfrac{\alpha f_{yo}}{f_{ck}} \quad \alpha = \dfrac{A_{so}}{A_c} \quad \Omega = \dfrac{A_c}{A_c + A_k} \quad A_k = 0.25\pi D_i \quad f_{ck} = 0.67 f_c'/0.8$
	$f_{cc}' = \gamma_c f_c' + 4.1 f_{rp,se}'$
	$\gamma_c = 1.85(D_o - 2t_o)^{-0.135} \quad \text{with}(0.85 \leq \gamma_c \leq 1.0)$
	$f_{rp,se}' = \begin{cases} 0.7(v_e - 0.5)\dfrac{2t_o}{D_o - 2t_o}f_{yo} & \text{if } D_o/t_o \leq 47 \\ \left(0.006241 - 0.0000357\dfrac{D_o}{t_o}\right)f_{yo} & \text{if } 47 < D_o/t_o < 150 \end{cases}$
	$v_e = 0.2312 + 0.3582 v_e' - 0.1524(f_c'/f_{yo}) + 4.843 v_e'(f_c'/f_{yo}) - 9.169(f_c'/f_{yo})^2$
	$v_e' = 0.881 \times 10^{-6}(D_o/t_o)^3 - 2.58 \times 10^{-4}(D_o/t_o)^2 + 1.953 \times 10^{-2}(D_o/t_o) + 0.4011$
Liang[4]	$N_{u,Liang} = (\gamma_c f_c' + 4.1 f_r)A_c + \gamma_{so}A_{so}f_{yo} + \gamma_{si}A_{si}f_{yi}$
	$f_r = 8.525 - 0.166\rho - 0.00897\tau + 0.00125\rho^2 + 0.00246\rho\tau - 0.0055\tau^2 \geq 0$
	$\gamma_c = 1.85(0.5D_o - t_o - 0.5D_i)^{-0.135} \quad \text{with}(0.85 \leq \gamma_c \leq 1.0)$
	$\rho = D_o/t_o \quad \tau = D_i/t_i$
	$\gamma_{so} = 1.458\rho^{-0.1} \quad \text{with}(0.9 \leq \gamma_{so} \leq 1.1)$
	$\gamma_{si} = 1.458\tau^{-0.1} \quad \text{with}(0.9 \leq \gamma_{si} \leq 1.1)$
Yan and Zhao[8]	$N_{u,Yan} = A_c f_c'(1 + \eta_c) + A_{so}f_{yo} + A_{si}f_{yi}$
	$\eta_c = \left(1.2 - 0.5\left(\dfrac{D_i}{D_o}\right)^2\right)\left(\dfrac{t_o}{D_o}\right)^{0.76}\dfrac{f_{yo}}{f_c'}$
Uenaka et al.[12]	$N_{u,Uenaka} = A_c f_c' + (2.86 - 2.59(D_i/D_o))A_{so}f_{yo} + A_{si}f_{yi} \quad \text{with}\left(0.2 \leq \dfrac{D_i}{D_o} \leq 0.7\right)$

Fig. 25. Comparison between the results of the design equations and actual values for short and slender columns (modified codes).
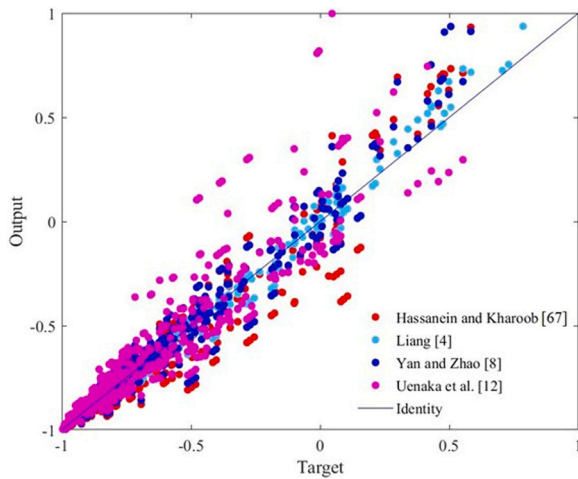

Fig. 26. Comparison between the results of the design equations and actual values for short columns (various design equations).
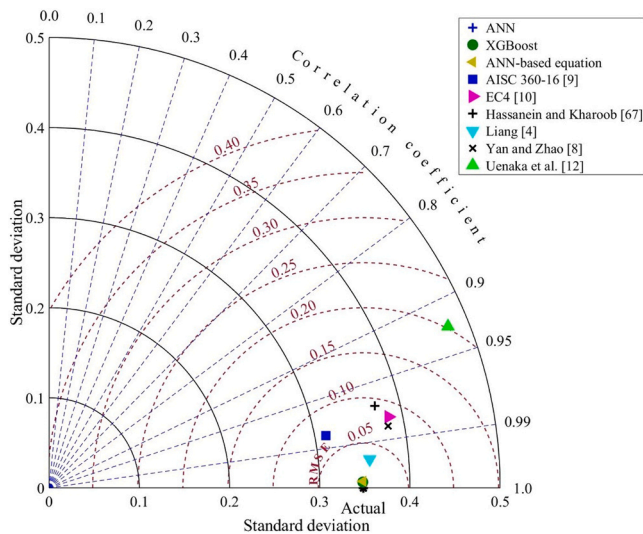

Fig. 27. Taylor diagram.

used to train and test the ML models. The performance of the developed ML models was evaluated using evaluation metrics. Based on the developed ML models, an ANN-based equation, MATLAB-based and Python-based GUIs were also developed to predict the ultimate axial capacity of CFDST short and slender columns. The prediction accuracy of the developed ML models and the proposed ANN-based equation was compared with that of six different design equations for CFDST columns. The following conclusions can be drawn:

1. The confinement effect provided by the outer and inner steel tubes on the sandwiched concrete should be considered in the FE modelling of CFDST columns.
2. Although both ANN and XGBoost models are capable of accurately predicting the ultimate axial capacity of CFDST columns, the ANN model has better generalization performance with lower RMSE for the test set.
3. The developed ML algorithms account for the effects of geometric and material parameters on the strengths of CFDST columns so that the outputs are reliable.
4. The diameter of the outer steel tube and the yield strength of the inner tube have the highest and lowest effects on the ultimate axial capacity of CFDST columns, respectively.
5. The developed ML models and the proposed ANN-based equation exhibit superior predictive performance over the other design formulas.

Finally, it is noteworthy that there is a limited data in the literature for CFDST slender column with non-compact and slender sections. Therefore, this is recommended as a subject for further study. It is also recommended that ML models should be developed for predicting the ultimate axial capacity of CFDST columns with geometric and material properties beyond the limits specified in Table 5.

CRediT authorship contribution statement

Zarringol Mohammadreza: Writing – original draft, Software, Methodology, Investigation, Formal analysis. **Liang Qing Quan:** Writing – review & editing, Supervision, Conceptualization. **Patel Vipulkumar:** Writing – review & editing, Supervision, Conceptualization. **Ahmed Mizan:** Writing – review & editing, Supervision, Conceptualization. **Hassanein Mostafa Fahmi:** Writing – review & editing, Supervision, Conceptualization.

Declaration of Competing Interest

The authors whose names are listed immediately below certify that they have NO affiliations with or involvement in any organization or entity with any financial interest (such as honoraria; educational grants; participation in speakers' bureaus; membership, employment, consultancies, stock ownership, or other equity interest; and expert testimony or patent-licensing arrangements), or non-financial interest (such as personal or professional relationships, affiliations, knowledge or beliefs) in the subject matter or materials discussed in this manuscript.

Data availability

All data, models, and code generated or used during the study appear in the published article.

Appendix A. Numerical example

In this Appendix, a numerical example is presented to calculate the ultimate capacity of a CFDST columns using the proposed ANN-based equations. The geometry and material properties of the columns are

as follows:

D_o= 250 (mm), t_o= 5 (mm), D_i= 50 (mm), t_i= 2.5 (mm), L= 750 (mm), f_{yo}= 300 (MPa), f_{yi}= 250 (MPa), $f_c^{'}$= 40 (MPa).

Since the geometric and material parameters of the column are within the limits specified in Table 5, the proposed ANN-based equation can be used as follows:

$$Q1 = [(-8428 \times 250) + (36254 \times 5) + (-63891 \times 50) + (147746 \times 2.5) + (934 \times 750) + (-111 \times 300) + (-4517 \times 250) + (52443 \times 40) + (13947611)]$$
$$\times 10 - 7$$
$$= 3.95423$$
(8)

$$Q2 = [(-3163 \times 250) + (-362813 \times 5) + (-139595 \times 50) + (2322523 \times 2.5) + (3935 \times 750) + (-12776 \times 300) + (1055 \times 250) + (195190 \times 40) + (-21594234)] \times 10 - 7$$
$$= 1.16231$$
(9)

$$Q3 = [(-90290 \times 250) + (-431056 \times 5) + (32726 \times 50) + (-590897 \times 2.5) + (212 \times 750) + (-20663 \times 300) + (-197 \times 250) + (-16546 \times 40) + (70342225)] \times 10 - 7$$
$$= 50.51379$$
(10)

$$Q4 = [(54845 \times 250) + (-118741 \times 5) + (-176041 \times 50) + (2190155 \times 2.5) + (1149 \times 750) + (5886 \times 300) + (605 \times 250) + (3138 \times 40) + (-17394285)]$$
$$\times 10 - 7$$
$$= 1.62506$$
(11)

$$Q5 = [(-43074 \times 250) + (254052 \times 5) + (-7765 \times 50) + (2299537 \times 2.5) + (605 \times 750) + (-1446 \times 300) + (-3874 \times 250) + (7112 \times 40) + (28568226)]$$
$$\times 10 - 7$$
$$= 11.76878$$
(12)

$$Q6 = [(47832 \times 250) + (-296667 \times 5) + (-104606 \times 50) + (-1040395 \times 2.5) + (589 \times 750) + (4937 \times 300) + (-6905 \times 250) + (-13226 \times 40) + (-7880016)] \times 10 - 7$$
$$= 1.57298$$
(13)

$$Q7 = [(12517 \times 250) + (-1383448 \times 5) + (44299 \times 50) + (-409650 \times 2.5) + (2586 \times 750) + (-11020 \times 300) + (751 \times 250) + (11143 \times 40) + (-23007740)] \times 10 - 7$$
$$= 1.07181$$
(14)

$$Q8 = [(44269 \times 250) + (-440401 \times 5) + (-56866 \times 50) + (170439 \times 2.5) + (-1059 \times 750) + (21733 \times 300) + (19146 \times 250) + (6773 \times 40) + (-3121339)] \times 10 - 7$$
$$= 5.09996$$
(15)

$$Q9 = [(-42569 \times 250) + (1295417 \times 5) + (36244 \times 50) + (-484439 \times 2.5) + (-1129 \times 750) + (-26067 \times 300) + (876 \times 250) + (3411 \times 40) + (22278986)] \times 10 - 7$$
$$= 3.83021$$
(16)

$$Q10 = [(46724 \times 250) + (-2139939 \times 5) + (-43376 \times 50) + (817662 \times 2.5) + (-182 \times 750) + (19379 \times 300) + (3699 \times 250) + (-20260 \times 40) + (-21665754)] \times 10 - 7$$
$$= 1.22274$$
(17)

$$Q11 = [(-116499 \times 250) + (284860 \times 5) + (89641 \times 50) + (232961 \times 2.5) + (437 \times 750) + (-1768 \times 300) + (980 \times 250) + (89016 \times 40) + (-9900236)]$$
$$\times 10 - 7$$
$$= 1.05539$$
(18)

$$Q12 = [(55250 \times 250) + (-223398 \times 5) + (-27071 \times 50) + (-427074 \times 2.5) + (-1176 \times 750) + (2807 \times 300) + (193 \times 250) + (24585 \times 40) + (-29057135)] \times 10 - 7$$
$$= 1.16879$$
(19)

$$Q13 = [(-46721 \times 250) + (811512 \times 5) + (34687 \times 50) + (-495644 \times 2.5) + (-1344 \times 750) + (-39830 \times 300) + (663 \times 250) + (1379$$
$$\times 40) + (31647649)] \times 10 - 7$$
$$= 4.24921 \tag{20}$$

$$Q14 = [(-13797 \times 250) + (99 \times 5) + (-14428 \times 50) + (14039 \times 2.5) + (558 \times 750) + (-6089 \times 300) + (15223 \times 250) + (1099 \times 40) + (10662698)]$$
$$\times 10 - 7$$
$$= 3.45203 \tag{21}$$

$$Q15 = [(18888 \times 250) + (182704 \times 5) + (-83539 \times 50) + (856886 \times 2.5) + (935 \times 750) + (2444 \times 300) + (-56 \times 250) + (-3409 \times 40) + (-11426681)]$$
$$\times 10 - 7$$
$$= 1.51987 \tag{22}$$

$$Q16 = [(-32024 \times 250) + (-209897 \times 5) + (114328 \times 50) + (-659914 \times 2.5) + (1940 \times 750) + (1282 \times 300) + (-822 \times 250) + (-3813$$
$$\times 40) + (4197834)] \times 10 - 7$$
$$= 2.07149 \tag{23}$$

$$Q17 = [(-2128 \times 250) + (43432 \times 5) + (26665 \times 50) + (455930 \times 2.5) + (-174 \times 750) + (3230 \times 300) + (-22586 \times 250) + (5130 \times 40) + (-4135105)]$$
$$\times 10 - 7$$
$$= 1.51790 \tag{24}$$

$$Q18 = [(24978 \times 250) + (-1281684 \times 5) + (161260 \times 50) + (-2856354 \times 2.5) + (-13 \times 750) + (6493 \times 300) + (-3060 \times 250) + (9954$$
$$\times 40) + (2814533)] \times 10 - 7$$
$$= 2.67264 \tag{25}$$

$$Q19 = [(62240 \times 250) + (-855851 \times 5) + (-25003 \times 50) + (270801 \times 2.5) + (546 \times 750) + (-8656 \times 300) + (-55 \times 250) + (21688$$
$$\times 40) + (-9666845)] \times 10 - 7$$
$$= 1.97115 \tag{26}$$

$$Q20 = [(-92834 \times 250) + (149409 \times 5) + (33394 \times 50) + (-17275 \times 2.5) + (258 \times 750) + (356 \times 300) + (161 \times 250) + (58310 \times 40) + (18028744)]$$
$$\times 10 - 7$$
$$= 1.98676 \tag{27}$$

$$N_u = 218774 + \sum_{j=1}^{20} \frac{Y_j}{1 + EXP(Q_j)}$$
$$= 218774 + \frac{-59487}{1 + EXP(3.95423)} + \frac{-6421}{1 + EXP(1.16231)} + \frac{43520}{1 + EXP(50.51379)} + \frac{-40751}{1 + EXP(1.62506)} + \frac{-121813}{1 + EXP(11.76878)} + \frac{-42695}{1 + EXP(1.57298)}$$
$$+ \frac{-26637}{1 + EXP(1.07181)} + \frac{-27863}{1 + EXP(5.09996)} + \frac{-87135}{1 + EXP(3.83021)} + \frac{-30484}{1 + EXP(1.22274)} + \frac{30896}{1 + EXP(1.05539)} + \frac{-153798}{1 + EXP(1.16879)} + \frac{42481}{1 + EXP(4.24921)}$$
$$+ \frac{-167592}{1 + EXP(3.45203)} + \frac{181279}{1 + EXP(1.51987)} + \frac{-49091}{1 + EXP(2.07149)} + \frac{-95953}{1 + EXP(1.51790)} + \frac{19781}{1 + EXP(2.67264)} + \frac{49277}{1 + EXP(1.97115)} + \frac{42114}{1 + EXP(1.98676)}$$
$$= 3594.8(kN) \tag{28}$$

The small difference between the results of the ANN-based equation and GUI (see Fig. 23) is that the equation has been rounded without decimals.

Appendix B. Supporting information

Supplementary data associated with this article can be found in the online version at doi:10.1016/j.engstruct.2024.117593.

References

[1] Du Y, Mohammed A, Chen Z, Al-Haaj M, Huang J. Seismic behaviors of CFT-column frame-four-corner bolted connected buckling-restrained steel plate shear walls using ALC/RAC panels. Thin-Walled Struct 2024;195:111365.

[2] Yang B, Shen L, Chen K, Feng C, Lin X, Elchalakani M, et al. Mechanical performance of circular ultrahigh-performance concrete–filled double skin high-strength steel tubular stub columns under axial compression. J Struct Eng 2022; 148:04021298.

[3] Li W, Ren Q-X, Han L-H, Zhao X-L. Behaviour of tapered concrete-filled double skin steel tubular (CFDST) stub columns. Thin-Walled Struct 2012;57:37–48.

[4] Liang QQ. Nonlinear analysis of circular double-skin concrete-filled steel tubular columns under axial compression. Eng Struct 2017;131:639–50.

[5] Ahmed M, Liang QQ, Patel VI, Hadi MNS. Computational simulation of eccentrically loaded circular thin-walled concrete-filled double steel tubular slender columns. Eng Struct 2020;213:110571.

[6] Li W, Cai Y-X. Performance of CFDST stub columns using high-strength steel subjected to axial compression. Thin-Walled Struct 2019;141:411–22.

[7] Yan X-F, Zhao Y-G, Lin S. Compressive behaviour of circular CFDST short columns with high- and ultrahigh-strength concrete. Thin-Walled Struct 2021;164:107898.

[8] Yan X-F, Zhao Y-G. Compressive strength of axially loaded circular concrete-filled double-skin steel tubular short columns. J Constr Steel Res 2020;170:106114.

[9] AISC. Specification for structural steel buildings. AISC 360–16. Chicago 2016.

[10] EC 4. Design of composite steel and concrete structures - Part 1–1: general rules and rules for buildings. EN 1994- 1–1 Eurocode 4. European Committee for Standardization, Brussels 2004.

[11] AS/NZS 5100.6. Bridge design, part 6: steel and composite construction. Standards Australia, Sydney, Australia 2017.

[12] Uenaka K, Kitoh H, Sonoda K. Concrete filled double skin circular stub columns under compression. Thin-Walled Struct 2010;48:19–24.

[13] Hassanein MF, Kharoob OF, Liang QQ. Circular concrete-filled double skin tubular short columns with external stainless steel tubes under axial compression. Thin-Walled Struct 2013;73:252–63.

[14] Truong V-H, Pham H-A, Huynh Van T, Tangaramvong S. Evaluation of machine learning models for load-carrying capacity assessment of semi-rigid steel structures. Eng Struct 2022;273:115001.

[15] Zhou X-G, Hou C, Peng J, Yao G-H, Fang Z. Structural mechanism-based intelligent capacity prediction methods for concrete-encased CFST columns. J Constr Steel Res 2023;202:107769.

[16] Degtyarev VV, Thai H-T. Design of concrete-filled steel tubular columns using data-driven methods. J Constr Steel Res 2023;200:107653.

[17] Hou C, Zhou X-G. Strength prediction of circular CFST columns through advanced machine learning methods. J Build Eng 2022;51:104289.

[18] Zarringol M, Thai H-T, Thai S, Patel V. Application of ANN to the design of CFST columns. Structures 2020;28:2203–20.

[19] Naser MZ, Thai S, Thai H-T. Evaluating structural response of concrete-filled steel tubular columns through machine learning. J Build Eng 2020;101888.

[20] Zhou X-G, Hou C, Feng W-Q. Optimized data-driven machine learning models for axial strength prediction of rectangular CFST columns. Structures 2023;47:760–80.

[21] Ren Q, Shen Y, Li M. Hybrid intelligence approach for performance estimation of rectangular CFST columns under different loading conditions. Structures 2022;39:720–38.

[22] Joo MR, Sofi FA. Unified Approach for Estimating Axial-Load Capacity of Concrete-Filled Double-Skin Steel Tubular Columns of Multiple Shapes Using Nonlinear FE Models and Artificial Neural Networks. Pract Period Struct Des Constr 2023;28:04022074.

[23] Mansur MA, Islam MM. Interpretation of Concrete Strength for Nonstandard Specimens. J Mater Civ Eng 2002;14:151–5.

[24] ABAQUS. Standard user's manual, version 6.12. Providence, RI (USA): Dassault Systemes Corp. 2012.

[25] Hassanein MF, Silvestre N, Yan X-F. Confinement-based direct design of circular concrete-filled double-skin normal and high strength steel short columns. Thin-Walled Struct 2023;183:110446.

[26] Tao Z, Han L-H, Zhao X-L. Behaviour of concrete-filled double skin (CHS inner and CHS outer) steel tubular stub columns and beam-columns. J Constr Steel Res 2004;60:1129–58.

[27] Yuan W-b, Yang J-j. Experimental and numerical studies of short concrete-filled double skin composite tube columns under axially compressive loads. J Constr Steel Res 2013;80:23–31.

[28] Wang W-D, Fan J-H, Shi Y-L, Xian W. Research on mechanical behaviour of tapered concrete-filled double skin steel tubular members with large hollow ratio subjected to bending. J Constr Steel Res 2021;182:106689.

[29] Han L-H, Yao G-H, Tao Z. Performance of concrete-filled thin-walled steel tubes under pure torsion. Thin-Walled Struct 2007;45:24–36.

[30] Patel VI, Liang QQ, Hadi MNS. Numerical analysis of circular double-skin concrete-filled stainless steel tubular short columns under axial loading. Structures 2020;24:754–65.

[31] Hassanein MF, Elchalakani M, Karrech A, Patel VI, Daher E. Finite element modelling of concrete-filled double-skin short compression members with CHS outer and SHS inner tubes. Mar Struct 2018;61:85–99.

[32] Huang H, Han L-H, Tao Z, Zhao X-L. Analytical behaviour of concrete-filled double skin steel tubular (CFDST) stub columns. J Constr Steel Res 2010;66:542–55.

[33] Wang J, Cheng X, Wu C, Hou C-C. Analytical behavior of dodecagonal concrete-filled double skin tubular (CFDST) columns under axial compression. J Constr Steel Res 2019;162:105743.

[34] Thai H-T, Uy B, Khan M, Tao Z, Mashiri F. Numerical modelling of concrete-filled steel box columns incorporating high strength materials. J Constr Steel Res 2014;102:256–65.

[35] FIP. CEB-FIP Model Code 1990. London: Thomas Telford Ltd.; 1993.

[36] AS 3600. Concrete structures. Standards Australia, Sydney, Australia 2009.

[37] Tao Z, Wang Z-B, Yu Q. Finite element modelling of concrete-filled steel stub columns under axial compression. J Constr Steel Res 2013;89:121–31.

[38] Pagoulatou M, Sheehan T, Dai XH, Lam D. Finite element analysis on the capacity of circular concrete-filled double-skin steel tubular (CFDST) stub columns. Eng Struct 2014;72:102–12.

[39] Yang Y-F, Fu F, Bie X-M, Dai X-H. Axial compressive behaviour of CFDST stub columns with large void ratio. J Constr Steel Res 2021;186:106892.

[40] Essopjee Y, Dundu M. Performance of concrete-filled double-skin circular tubes in compression. Compos Struct 2015;133:1276–83.

[41] Fan J, Baig M, Nie J. Test and analysis on double-skin concrete filled tubular columns. Tubul Struct XII: Proc Tubul Struct XII, Shanghai, China, 8-10 2008;2008:407.

[42] Lu H, Zhao X-L, Han L-H. Testing of self-consolidating concrete-filled double skin tubular stub columns exposed to fire. J Constr Steel Res 2010;66:1069–80.

[43] Ayough P, Ibrahim Z, Ramli Sulong NH, Ganasan R, Hamad Ghayeb H, Elchalakani M. Experimental and numerical investigations into the compressive behaviour of circular concrete-filled double-skin steel tubular columns with bolted shear studs. Structures 2022;46:880–98.

[44] Zhao X-L, Tong L-W, Wang X-Y. CFDST stub columns subjected to large deformation axial loading. Eng Struct 2010;32:692–703.

[45] Wang J, Shen Q, Wang F, Wang W. Experimental and analytical studies on CFRP strengthened circular thin-walled CFST stub columns under eccentric compression. Thin-Walled Struct 2018;127:102–19.

[46] Pedregosa F, Varoquaux G, Gramfort A, Michel V, Thirion B, Grisel O, et al. Scikit-learn: Machine learning in Python. the Journal of machine Learning research 2011;12:2825–30.

[47] MATLAB. MATLAB (R2018b). The MathWorks Inc., Natick, Massachusetts, USA. 2018.

[48] Chen T., Carlos G. A scalable tree boosting system. in: Proceedings of the 22nd ACM SIGKDD International Conference on Knowledge Discovery and Data Mining 2016:85–794.

[49] Friedman JH. Greedy Function Approximation: A Gradient Boosting Machine. Ann Stat 2001;29:1189–232.

[50] Zhao X-Y, Chen J-X, Wu B. An interpretable ensemble-learning-based open source model for evaluating the fire resistance of concrete-filled steel tubular columns. Eng Struct 2022;270:114886.

[51] Lundberg SM, Lee S-I. A unified approach to interpreting model predictions. Adv Neural Inf Process Syst 2017:30.

[52] Shapley LS. A value for n-person games. Contrib Theory Games 1953;2:307–17.

[53] Feng D-C, Wang W-J, Mangalathu S, Hu G, Wu T. Implementing ensemble learning methods to predict the shear strength of RC deep beams with/without web reinforcements. Eng Struct 2021;235:111979.

[54] Nguyen H, Vu T, Vo TP, Thai H-T. Efficient machine learning models for prediction of concrete strengths. Constr Build Mater 2021;266:120950.

[55] Bakouregui AS, Mohamed HM, Yahia A, Benmokrane B. Explainable extreme gradient boosting tree-based prediction of load-carrying capacity of FRP-RC columns. Eng Struct 2021;245:112836.

[56] Wakjira TG, Ibrahim M, Ebead U, Alam MS. Explainable machine learning model and reliability analysis for flexural capacity prediction of RC beams strengthened in flexure with FRCM. Eng Struct 2022;255:113903.

[57] Cakiroglu C, Islam K, Bekdaş G, Isikdag U, Mangalathu S. Explainable machine learning models for predicting the axial compression capacity of concrete filled steel tubular columns. Constr Build Mater 2022;356:129227.

[58] Wang C, Chan T-M. Machine learning (ML) based models for predicting the ultimate strength of rectangular concrete-filled steel tube (CFST) columns under eccentric loading. Eng Struct 2023;276:115392.

[59] Thai H-T. Machine learning for structural engineering: A state-of-the-art review. Structures 2022;38:448–91.

[60] Zarringol M, Patel VI, Liang QQ. Artificial neural network model for strength predictions of CFST columns strengthened with CFRP. Eng Struct 2023;281:115784.

[61] Zarringol M, Thai H-T, Naser MZ. Application of machine learning models for designing CFCFST columns. J Constr Steel Res 2021;185:106856.

[62] Du Y, Chen Z, Zhang C, Cao X. Research on axial bearing capacity of rectangular concrete-filled steel tubular columns based on artificial neural networks. Front Comput Sci 2017;11:863–73.

[63] Yavuz Bayraktar O, Salem Taher Eshtewı S, Benli A, Kaplan G, Toklu K, Gunek F. The impact of RCA and fly ash on the mechanical and durability properties of polypropylene fibre-reinforced concrete exposed to freeze-thaw cycles and MgSO4 with ANN modeling. Constr Build Mater 2021;313:125508.

[64] Chen W, Xu J, Dong M, Yu Y, Elchalakani M, Zhang F. Data-driven analysis on ultimate axial strain of FRP-confined concrete cylinders based on explicit and implicit algorithms. Compos Struct 2021;268:113904.

[65] Nguyen MST, Kim S-E. A hybrid machine learning approach in prediction and uncertainty quantification of ultimate compressive strength of RCFST columns. Constr Build Mater 2021;302:124208.

[66] Liang QQ. Numerical simulation of high strength circular double-skin concrete-filled steel tubular slender columns. Eng Struct 2018;168:205–17.

[67] Hassanein MF, Kharoob OF. Compressive strength of circular concrete-filled double skin tubular short columns. Thin-Walled Struct 2014;77:165–73.

[68] Deng R, Zhou X-H, Deng X-W, Ke K, Bai J-L, Wang Y-H. Compressive behaviour of tapered concrete-filled double skin steel tubular stub columns. J Constr Steel Res 2021;184:106771.

[69] Li W, Han L-H, Zhao X-L. Axial strength of concrete-filled double skin steel tubular (CFDST) columns with preload on steel tubes. Thin-Walled Struct 2012;56:9–20.

[70] Taylor KE. Summarizing multiple aspects of model performance in a single diagram. J Geophys Res: Atmospheres 2001;106:7183–92.

[71] Zarringol M, Thai H-T. Prediction of the load-shortening curve of CFST columns using ANN-based models. J Build Eng 2022;51:104279.

[72] Goode C.D.. Composite columns - 1819 tests on concrete-filled steel tube columns compared with Eurocode 4. 2008;86:33–38.